

IISc THESES ABSTRACTS

Thesis Abstract (Ph.D.)

Microbial emulsification and metabolism of organophosphorous pesticides by Mukul N. Patel.

Research supervisor: K. P. Gopinathan.

Department: Microbiology and Cell Biology.

1. Introduction

Pesticides form an integral and indispensable part of the world agriculture. The application of pesticides has not only increased the total and the average per hectare yields, but also controlled various vector-borne diseases. Despite these benefits there are significant risks associated with the increased usage of pesticides resulting in environmental pollution affecting all forms of life. Human poisoning is the highest price paid. Stringent laws governing the safe use of pesticides have been implemented in various countries. Highly toxic or persistent pesticides such as organochlorines and mercurials have been banned or their use restricted in most of the advanced countries. The current emphasis, therefore, is on the use and development of biodegradable non-persistent and less toxic alternatives.

Organophosphorous pesticides have been used increasingly over the last decade as replacement for the more persistent organochlorine and mercurial pesticides¹. They are susceptible to chemical and biological degradation in the environment. Even though microbial attack on organophosphorous pesticides is well documented, only in a few cases the routes and intermediates have been elucidated². This is mainly because of the low solubility/miscibility of these pesticides in water and their toxic nature. Many microorganisms produce bioemulsifiers or biosurfactants during their growth on insoluble compounds such as hydrocarbons, elemental sulfur and 2,4,5-T^{3,4}. At least in certain cases the emulsification process seems to be a prelude to their subsequent degradation. The present investigation describes, for the first time, the isolation and characterization of microbial emulsifier specific to immiscible organophosphorous pesticides⁵.

2. Isolation and characterization of bacteria capable of emulsification of pesticides

Two bacterial strains capable of emulsifying immiscible organophosphorous pesticides were isolated from a fenthion enrichment culture. These bacterial strains were identified as *Bacillus subtilis* diverge forms based on various morphological, cultural and biochemical characteristics. The emulsifying activity from one of these strains, namely, *B. subtilis* FE-2 was studied in detail.

3. Physiology and characterization of emulsifying agent

Optimal conditions for the assay of emulsification of pesticides were standardised. The emulsifying agent was constitutively produced by the bacterium, whether or not grown in the presence of pesticide. It was released in the cultures when grown on 0.05% pesticide, 0.05% glucose or 10 mM succinate. The emulsifying activity was released by the cultures when grown in Luria broth or 1% glucose only when the pesticide (fenthion) was present in the medium and under high agitation conditions. The emulsifying agent was nondialysable and did not require any dialysable factors or metal ions for its activity. Buffering the solution to pH 7.0-7.6 was necessary to obtain the activity. The emulsifying agent could be precipitated with trichloroacetic acid and ammonium sulphate. It was thermostable, partially extracted by some solvents, partially sensitive to proteases and phospholipase C and highly sensitive to lysozyme and SP 249 (another enzyme acting on carbohydrate moieties). The emulsifier may, therefore, be a macromolecule, glycolipopeptide in nature.

The emulsifier was highly specific to immiscible organophosphorous pesticides. Maximal emulsification was observed at pH values 7.0-7.6. It did not emulsify other insoluble or immiscible organic compounds such as organochlorine pesticides and hydrocarbons. On treatment of the crude emulsifier preparations with lysozyme, the emulsifying activity was lost. Such lysozyme-treated preparations, when subjected to electrophoresis on polyacrylamide gels, showed the disappearance of a particular protein band. The corresponding protein band in the untreated preparations when extracted from the gels showed emulsifying activity. The disappearance of the protein band on acrylamide gel electrophoresis consequent to treatment of emulsifier with lysozyme was observed under both non-denaturing and denaturing conditions. The protein band had an apparent molecular weight of 43,000. The interaction of lysozyme with the emulsifier appeared to be ionic in nature. Besides, lysozyme addition to the preformed emulsions resulted in the breakage of the emulsion. Deemulsification could be brought about by other positively charged molecules also.

The emulsifier (M_r 43,000) was purified by ion-exchange chromatography on DEAE-Sephacel and gel filtration on Sephacryl S-200 about 50 fold and with a yield of 4%.

4. Metabolism of pesticide

Bacillus subtilis FE-2 metabolises fenitrothion by more than one pathway—reductive and hydrolytic. Apart from 3-methyl-4-nitrophenol (product of fenitrothion hydrolysis) and amino fenitrothion (product of fenitrothion reduction), it forms other chloroform soluble and highly polar metabolites. However, the rate of fenitrothion metabolism is low, at least by the hydrolytic pathway. Only a low level of $^{14}\text{CO}_2$ is generated from [^{14}C] fenitrothion. Thus, in the case of *Bacillus subtilis* FE-2 there is no correlation between its ability to emulsify and the extent of degradation of immiscible organophosphorous pesticides. Therefore, the emulsification may have some other role for producing the strain. It is likely that *B. subtilis* FE-2 is a member of mutualistic community acting on organophosphorous pesticides and other xenobiotics in the natural environment.

The emulsifying agent described in the present investigation has potential applications both in pesticide formulations and pesticide disposal. It could be exploited for the removal and the recovery of pesticides and in controlled delivery systems.

References

- MULBRY, W. W., KARNS, J. S., KEARNEY, P. C., NELSON, J. O., MCDANIEL, C. S. AND WILD, J. R. *Appl. Environ. Microbiol.*, 1986, **51**, 926-935.
- LAL, R. *Adv. Appl. Microbiol.*, 1982, **26**, 229-253.
- CIRIGLIANO, M. C. AND CARMAN, G. M. *Appl. Environ. Microbiol.*, 1984, **48**, 747-750.
- BANERJEE, S., DASGUPTA, S. AND CHAKRABARTY, A. M. *Arch. Microbiol.*, 1983, **135**, 110-114.
- PATEL, M. N. AND GOPINATHAN, K. P. *Appl. Environ. Microbiol.*, 1986, **52**, 1224-1226.

Thesis Abstract (Ph.D.)

Mechanism of electroreduction of nitrobenzene in alkaline media by K. Kannan.

Research supervisors: S. Soundararajan and S. K. Vijayalakshamma.

Department: Inorganic and Physical Chemistry.

1. Introduction

Many studies have been conducted on the mechanism and end products of electroreduction of nitrobenzene^{1,2}. Prompted by earlier reports that the reduction of nitrobenzene in aprotic media occurs by a

reversible one-electron step to yield radical anion³ and four-electron step splits up into two steps in certain aqueous alkaline media⁴, effort is directed towards understanding the conditions which govern the mechanism of this reduction.

2. Results

A wide variety of organic solvents like ethanol, chloroethanol, ethoxy ethanol, THF, dioxan, acetonitrile, acetone, hexamethyl phosphoramide, DMF and DMSO are used as 40% solutions and ionic strength is varied between 0.2 and 1.1 molar, always maintaining alkali concentration as 0.2M. An examination of the polarograms in these different media shows that the first step of reduction is a single electron addition in every case. The product of this step, the free-radical anion PhNO_2^- is very reactive. It reacts with the components of the medium as follows:



In the present series of experiments, aqueous solvents with 40% organic components were used. The solvate formation (eqn 2) thus could involve either water or the organic solvent. If the solvating molecule is hydroxylic (ROH), the radical anion can abstract a proton from the solvent thus



If the solvating molecule is aprotic, the solvate still carries a negative charge and resists further reduction but the PhNO_2H or the ion pair can be reduced more easily.

2.1. Aprotic solvents

In media containing 40% acetonitrile, acetone, tetra-hydrofuran, dioxan and hexamethyl phosphoramide (solvents of high acceptor number), the radical anion is preferentially solvated by the organic solvent even in the presence of excess of water molecules. So in these solvent mixtures with low ionic strength, the stability of the free radical solvate makes the reduction occur in two separate steps. However, in the same media but higher ionic strength, the probability of ion pair formation is higher and further reduction is favoured. Hence, as the ionic strength in the medium increases, the two steps come closer and finally merge together.

2.2. Hydroxylic solvents

Though solvents like DMF and DMSO have higher acceptor ability, they do not preferentially solvate the radical anion in aqueous solution. It is known that these two solvents can solvate cations more easily than they do solvate anions. Hence, in aqueous media containing DMF and DMSO, it is water molecules which solvate the free radical anion. In aqueous media of ethanol, ethoxy ethanol, chloroethanol, DMF and DMSO, hydroxylic solvates are formed, further reduction is favoured and so a single-step reduction is observed.

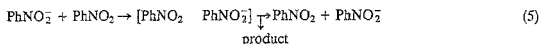
2.3. Reaction of free radical anion

In cases where two-step reduction occurs, linear sweep voltammetry shows that the first step is reversible and the second irreversible. The first step has been examined closely. A small anodic step corresponding to the oxidation of PhNO_2^- is seen in the reverse scan. The anodic height is not quantitative. It is quite small at lower scan rates but improves as the scan rate increases, thereby showing that in flow scan rate experiments, PhNO_2^- is being lost in the large time gap between its formation and detection.

As long as the potential is not allowed to go more negative than the first step, no other product is indicated. However, if the potential crosses the second step, the anodic sweep shows the step due to the oxidation of phenyl hydroxyl amine. The same products are seen in media which give single four-electron

wave. Here also an anodic step due to oxidation of PhNO_2^- is seen. Whether the reduction occurs in a single step or in two steps, the reduction is mainly a non-electron reaction followed by a 3-electron step. The primary product of the total reduction is always phenyl hydroxyl amine. In the presence of dissolved oxygen or in the course of intermittent oxidation and reduction, the primary product is converted to azoxy benzene.

A study of the stepwise reduction by chromopotentiometry shows that the ratio of the step height of the second to the first step is varying with concentration. In acetonitrile and acetone, the ratio of $n_2:n_1$ is less than 3:1 at lower concentration of PhNO_2 and approach the value 3:1 at higher concentration. This indicates that there is some coupled chemical reaction between the two steps. The ratio of reduction to oxidation step height in the current reversal chromopotentiometry of the first step indicates that PhNO_2^- is being lost during the time scale of these experiments. Comparing the transition time constant with the theoretically expected value and examining it as a function of current density and time, the possible coupled reactions in addition to equations 2, 3 and 4 can be written as



and



2.4. DMSO as a solvent

Of the ten solvents studied, DMSO is unique in that there is evidence for two forms of phenyl hydroxyl amino and two forms of nitrobenzene in equilibrium in this medium. Probably one of them is solvated species and the other is unsolvated.

References

1. KEMULA, W. AND KRYGOWSKI, T. M. *Encyclopedia of electrochemistry of elements/Organic section* (ed. A. J. Bard), 1979, Ch. 2, Marcel Dekker.
2. SMITH, W. H. AND BARD, A. J. Electrochemical reactions of organic compounds in liquid ammonia, *J. Am. Chem. Soc.*, 1975, **97**, 5203-5210
3. MAKI, A. H. AND GESKE, D. H. Electron spin resonance and polarographic investigation of substituted nitrobenzene negative ions, *J. Am. Chem. Soc.*, 1961, **83**, 1852-1860.
4. HOLLECK, L., KASTENING, B. AND WILLIAMS, R. D. Uber die wirkungsweise von inhitoren bei polarographischer reduktion organischer verbindungen, *Z. Electrochem*, 1962, **66**, 396-401.

Thesis Abstract (Ph.D.)

New kinematic studies on the proportional navigation problem by U. S. Shukla.

Research supervisors: P. R. Mahapatra and N. Balakrishnan.

Department: Aerospace Engineering.

I. Introduction

The work concerns with the study of the kinematics of pursuer motion under Proportional Navigation (PN) law which has found wide practical usage in a number of realistic applications, especially in aerospace guidance systems. The aim of the study has been to derive explicit analytical solutions for the Pure Proportional Navigation (PPN) that are both accurate and versatile and are applicable for both non-maneuvering and maneuvering target cases. The solutions are valid over a wide range of engagement geometries and constitute a substantial qualitative and quantitative refinement over currently available classical linear solutions² which are valid only for near-tail-chase geometries.

2. The status of PN study

The current analytical insight into PN behavior, as obtained from published literature, is far from complete. The approach to solving the PN problem has been made hitherto along two principal directions. The prime difference between these two arises from the way PN is defined. While one class consists of PPN and its variants which are referenced with respect to pursuer velocity vector, the other class has LOS-referenced laws³ like True Proportional Navigation (TPN) and its generalizations as its members. From a point of view of mathematical analysis, it has been possible to solve the LOS-referenced laws in closed form (though the solutions are mostly implicit in nature) for at least the non-maneuvering target case. In contrast, PPN⁴ has been solved in closed form, for the non-maneuvering target, only for the less useful discrete values 1 and 2 of N . It has been shown in this work that notwithstanding the relative difficulties in solving the PPN problem, PPN (including its variants) is the most natural PN law and therefore deserves a closer study. This conclusion is drawn based on the facts that the LOS-referenced laws that are not practically implementable require forward acceleration/deceleration, are inefficient, lead to severe constraints on the initial engagement geometry to ensure acceptable trajectory behavior and intercept and are thus less robust. Also, the relative analytical advantage of LOS-referenced PN laws does not appear sustainable as more realistic PN scenarios are analyzed. The relative importance of PPN as also its relatively low level of mathematical development has been the prime motivation for this work and its major contributions fall in this area.

In the absence of closed-form solutions for the PPN problem, reliance has been placed on linearized solutions, although limited qualitative treatment is available that only establishes certain bounds on the trajectory behavior. The linear solutions are simple and useful, and have provided considerable insight into the PN system behavior. A systematic derivation is made in this work of the linear solution to serve as the basis for a uniform treatment and system of notation for application to the formulation. The linear solution also serves as a basic reference for assessing improvements resulting from the more refined treatments and helps in identifying the structural generalizations achieved.

3. Main results

Biased PN (BPN)⁵ is one of the variants that improves the efficiency of the basic PPN. The linear theory is extended to the treatment of BPN case and the performance of BPN is optimized to obtain the optimum bias value. It is shown through concrete examples of both atmospheric and extra-atmospheric engagement scenarios that control effort saving by a factor of as much as 3 is possible under realistic conditions through the use of optimum bias.

The work then concentrates on the development of analytical solutions for the PPN law which are valid over a wide range of engagement conditions. A quasilinear (QL)⁶ approach is used to approximate the original nonlinear PPN differential equations and the resulting single-iteration QL equations are solved in closed form. The explicit expressions so obtained for the trajectory parameters are found to yield very accurate results over a wide range of engagement geometries with a proper choice of initial approximation to the solution.

The issue of obtaining a good initial approximation is studied in detail. A sensitivity study has been carried out and an analytical optimization has been performed to obtain the best initial approximation at any point during the engagement. In addition, a set of heuristic choices for the initial approximations have also been made in view of their extreme logical simplicity. In particular, it has been shown that the choice of initial LOS angle as the initial approximation results in considerable simplification of the expressions for trajectory parameters while providing good accuracy of the results throughout the trajectory. The choice of such an initial approximation has reduced the QL solution to a generalized linear (GL) form which is further reduced through a weak application of the small-angle approximations, to obtain a solution which has the same form as the classical linear (CL) solution. However, the GL solution is found to be valid over a wide range of engagement geometries and is analytically shown to be a consistent generalization of the CL solution. The power of the GL solution derives from a generalization of the effective navigation constant of the CL solution.

While the main results of the analytical QL solution have been derived by considering only the first-order term in the Taylor's series expansion in function space, to study the improvement in accuracy and to gain insight into the convergence properties of the solution, a second-order QL solution has also been derived. The second-order solution, expectedly, gives further improvement in the accuracy and lends confidence regarding the convergence behavior of the QL solution. This solution is again shown to be a consistent generalization of the first-order QL solution.

This work also deals with the difficult case of PN guidance against a laterally maneuvering target. A perturbation technique is employed, in addition to quasilinearization process, to obtain an approximate solution in closed form. The solutions for all the important trajectory parameters have been obtained explicitly even for this complex case. The solution for maneuvering targets is shown to be valid over a wide range of engagement geometries, besides being valid for high target maneuvers also. A major feature of the approach used has been the establishment of a consistent hierarchy of explicit solutions in which structural similarity is maintained between solutions of various levels.

References

1. YUAN, C L Homing and navigational courses of automatic target-seeking devices, *J. Appl. Phys.*, 1948, **19**, 1112-1128
2. JERGER, J. J. *Systems preliminary design*, 1960, Van Nostrand
3. GUELMAN, M The closed form solution of true proportional navigation, *IEEE Trans.*, 1976, **AES-7**, 472-482.
4. LOCKE, A. S *Guidance*, 1956, D. Van Nostrand.
5. MURTAUGH, S. A. AND CRIEL, H. E. Fundamentals of proportional navigation, *IEEE Spectrum*, 1966, **3**, 75-85.
6. ALSAUGH, D. W. AND HALLUM, M. M *Quasilinearization solution of the proportional navigation*, Technical Report No RD-81-15, US Army Missile Command, Alabama, June 1981.

Thesis Abstract (Ph.D.)

Optimum constant-power compact pulse codes for rejection of range-Doppler radar clutter by T. K. Bhattacharya.

Research supervisors: N. Balakrishnan and P. R. Mahapatra.

Department: Aerospace Engineering.

1. Introduction

In most practical situations, the detection capability of a radar is more often limited by the presence of clutter than by noise. Conventionally, improved immunity to clutter or the clutter rejection is achieved by an appropriate design of either the receiver filter, the transmitter waveform or both. The ease of realization and the versatility to work in a wide variety of clutter environments which form the basis for most operational radars, favor the choice of transmitter waveform design for improving clutter rejection. Of the possible transmitter waveforms, those that involve frequency and phase modulations are capable of enhanced performance. However, a systematic design methodology to exploit such signals to offer enhanced performance in the presence of an *a priori* known clutter distribution, has not been evolved in the open literature so far. This work is a contribution towards bridging this gap.

The main thrust of this work is two fold. The first is to develop a versatile design methodology that offers enhanced detection capabilities of targets in clutter-limited environments. The second emphasis is to generate, for the first time, exhaustive numerical results that illustrate the extent of improvements in clutter rejection that are possible in typical target-clutter scenarios with frequency, phase and the combined frequency and phase modulated, compact pulse bursts.

The versatility of the methods developed in this work stems from the fact that clutter rejection is studied using complete information available from the ambiguity function in the delay-Doppler plane. The maximization of the performance criterion of SIR is first shown to reduce to that of minimization of the clutter integral. The clutter integral is a complex function of only the pulse burst parameters when a matched filter receiver is assumed. In this work, elegant mathematical expressions for the clutter integral have been obtained for all the signal families in such a way that the clutter integral is computationally convenient to evaluate. These expressions which are original to this work are only a first step towards making the signal design versatile. The ability of the design methodology reported here is enhanced by the use of Simplex method¹ which is a nonlinear optimization technique and has an inherent immunity to convergence to local minima. The latter aspect is very important since the clutter integral is a highly nonlinear function of the subpulse parameters. In brief, both the formulation of the clutter integral and the choice of minimization contribute to the versatility of the methods described. A brief review of the major results obtained is made here.

2. Clutter description

The most general and practically realistic description of the clutter distribution includes the delay-Doppler occupancy of the clutter. Depending on the causes, either natural or man-made, the clutter can have significant spread in both range and velocity. Such clutter distributions are described by a 2-D distribution in the delay-Doppler plane of the ambiguity function of the radar. The paucity of results in the literature that deal with arbitrary 2-D clutter scenarios is indicative of the importance of our work and almost all the formulations and the associated numerical results are reported here for the first time.

For illustrative purposes, seven 2-D clutter distributions pertaining to different possible practical situations have been considered. These distributions have distinct delay-Doppler extents and are used as testbeds for evaluating and comparing the clutter-rejection properties of the codes designed by us and also of other standard codes available in the literature. However, all the signal design techniques enumerated in this work are inherently capable of yielding optimum clutter rejection against any arbitrarily defined delay-Doppler extents of the clutter.

3.1. PSK pulse bursts

The performance of the PSK codes is studied in this work in the presence of arbitrary delay-Doppler clutter. The comparison of the optimum PSK codes generated is done with the popular Barker² and Frank³ codes, though the latter codes are only optimum against 1-D, zero-Doppler clutter only. Significant performance improvements, as compared to Barker and Frank codes, are obtained for all the seven clutter distributions. PSK bursts of lengths 5, 7, 13, 25 and 65 are considered to demonstrate the extent of improvement in clutter rejection that is possible with increase in burst length. Pulse bursts up to 65 pulses long were designed. This is an indication that the technique evolved by us is more than capable of handling realistic and practical radar signal design.

It is shown that the optimum PSK signal design yields codes with smaller burst length as compared to the Barker code for the same clutter-rejection property. For example, the optimum 7-pulse PSK burst is seen to have nearly the same clutter integral values as that of 13-pulse Barker code, for all the seven clutter distributions.

3.2. FSK bursts

FSK bursts can be designed to have larger bandwidths than the PSK bursts and hence they possess better clutter-rejection capabilities. In general, the maximum usable bandwidth of FSK bursts is limited to N^2 (N being the length of the pulse burst). Higher bandwidth than N^2 does not give performance improvement that is commensurate with the deterioration in SNR. The bandwidth available to the signal designer is limited further by other tactical requirements. Hence, to evolve a design methodology that has wide applicability, FSK bursts have been designed with the allowable bandwidth as a constraint.

The clutter integral values and the maximum sidelobe levels were also calculated for the codes described by Costas⁴, Mersereau *et al*⁵ and Titlebaum *et al*⁶ for the purpose of comparison. It is shown that the

optimum FSK codes are better than the above general-purpose codes for all seven clutter distributions.

The improved performance of FSK codes is shown to be even more apparent when the allowable signal bandwidth is reduced. This is attributed to the larger deterioration in the performance of Costas, Mersebau, and Titlebaum codes at lower signal bandwidths.

It is worth noting that the FSK design technique that works for 2-D clutter distributions and with a prespecified bandwidth has been developed for the first time and this has large practical utility.

3.3. P&FSK bursts

P&FSK bursts offer the possibility of a better control over the frequency spectrum occupied by the signal. This can, in certain situations, be used for improving the clutter-rejection properties of the signal. To this end, a design technique wherein both the frequency and phase of the subpulses are used as design variables is evolved. These signals are denoted as P&FSK bursts.

It is shown that when the available bandwidth is of the order of N^2 , the improvements in the clutter integral values of the P&FSK bursts are not significant as compared to the FSK bursts. However, for all the seven clutter distributions, the clutter integral values for the P&FSK bursts were shown to be significantly lower than that of FSK bursts, when the allowable bandwidth is reduced from N^2 . In effect, it is shown that simultaneous control over the phase and frequency of the subpulses is most effective whenever the allowable bandwidth is at a premium.

3.4 Integer PSK bursts

The practical realization of PSK bursts becomes simpler when the number of admissible phases is reduced to a few in number. To address such a class of requirements, a discrete or integer optimization technique is reported in this work and signals denoted as integer PSK bursts are designed.

Two practically attractive phase-coding schemes are used for illustration. They are the biphasic codes, with the admissible phases of $(0, \pi)$, and the quadriphase codes, with the admissible phases of $(0, \pi/2, \pi, 3\pi/2)$. An algorithm based on SUMT⁷ is shown to be effective in handling the restriction that the allowable phases are finite in number. The basic philosophy of the algorithm has been to convert the constrained optimization problem into a series of unconstrained optimization exercises. This has permitted the use of the Simplex method also to the integer PSK bursts. With this, all the attractive features of the Simplex method such as immunity to convergence to local minima are also retained in the integer PSK design.

It is shown that the optimum integer PSK signal design offers nearly the same performance as the continuous PSK codes for all the seven clutter distributions, even when the admissible phases are reduced to the biphasic set.

4. Conclusions

Thus, from the results obtained it can be concluded that the signal design methodology reported here is versatile to handle general 2-D clutter distributions. The advantages of using *a priori* knowledge about the delay-Doppler occupancy of the clutter in the signal design effort in a systematic manner have also been illustrated.

References

1. NELDER, J. A. AND MEAD, R. A Simplex method for function minimization, *Computer J.*, 1965, 7, 308-315.
2. BARKER, R. M. Group synchronizing of binary digital systems, in *Communication theory*, W. Jackson (ed.), 1953, pp 273-287, Academic Press.
3. FRANK, R. L. Polyphase codes with good nonperiodic correlation properties, *IEEE Trans.*, 1963, IT-9, 43-45

4. COSTAS, J. P. A study of a class of detection waveforms having nearly ideal range-Doppler ambiguity properties, *Proc. IEEE*, 1984, **72**, 996-1009.
5. MERSEREAU, R. M AND SEAY, T S Multiple access frequency hopping patterns with low ambiguity, *IEEE Trans.*, 1981, **AES-17**, 571-578
6. TITLEBAUM, E L. AND SIBUL, L. H. Time frequency hop signals, Part II: Coding based upon quadratic congruences, *IEEE Trans*, 1981, **AES-17**, 494-500.
7. FIACCO, A V AND McCORMICK, G P *Nonlinear programming Sequential unconstrained minimization techniques*, 1968, Wiley.

Thesis Abstract (Ph.D.)

Structure of turbulence in a neutrally stable atmospheric boundary layer by Sudarsh V. Kailas.

Research supervisors: R. Narasimha and Sulochana Gadgil.

Department: Aerospace Engineering.

1. Introduction

Ever since the discovery of bursts in a turbulent boundary layer¹, a variety of experimental studies have been carried out by many workers in an attempt at elucidating the nature of this phenomenon²⁻⁶. There have also been investigations of energy production in geophysical boundary layers⁷⁻¹⁰. However, these geophysical studies have generally not received the attention we believe they merit from laboratory fluid dynamicists, the reason in part being that the results are difficult to assess as the methods used have in general been different from those used in the laboratory. We, therefore, study here the atmospheric boundary layer using the well-known VITA technique¹¹ to detect events in the atmosphere which, besides being of use to atmospheric scientists in such problems as pollutant dispersion and mixing, evaporation in maritime boundary layer and transfer of heat and momentum across geophysical boundaries, could also shed light on the nature of the bursting phenomenon at high Reynolds numbers. In particular, data on the frequency of such events would be decisive because of the identity of wall scales in laboratory and atmospheric flows accompanied by a vast disparity ($1:10^4$) in the outer scales.

2. Mean flow variables and selection of data subsets

The data analysed were recorded at near-neutral conditions of stability on the 300 m instrumented tower at the Boulder Atmospheric Observatory (described by Kaimal and Gaynor²) and include all three velocity components measured by sonic anemometers, and temperature, at eight heights above ground.

A detailed study of the mean flow was useful in bringing out a qualitative similarity between the atmospheric and laboratory data, elucidating the large-scale flow conditions like stability characteristics, and identifying data subsets which were stationary and neutrally stable.

2.1. The VITA technique

The variable interval time average (VITA) technique, as developed by Blackwelder and Kaplan¹¹, defines a short-time variance D for any fluctuating turbulent quantity p' as

$$D(p'; t, t_{av}) = \frac{1}{t_{av}} \int_{t-t_{av}/2}^{t+t_{av}/2} p'^2(s) ds - \left(\frac{1}{t_{av}} \int_{t-t_{av}/2}^{t+t_{av}/2} p'(s) ds \right)^2$$

where t_{av} is a prescribed time interval of averaging. The mean square value of p' , defined as

$$\bar{p}^2 = \lim_{t_{av} \rightarrow \infty} D(p'; t, t_{av}),$$

is of course independent of t in steady flow.

When a peak in the short-time variance signal D exceeds a certain discriminator level $k\bar{p}^2$, where k is any prescribed threshold, we shall say that a 'special event' of intensity k has occurred.

2.2. Energy events

Events were detected from the u' signal (horizontal velocity) by applying VITA on various stretches of data, and the dependence of the event frequency on both k and t_{av} has been studied. These results show a remarkable similarity to those of Johansson and Alfredsson⁴ in a channel, but do not suggest any method of determining a unique event frequency. Similar results are obtained with vertical velocity and temperature. A study of the conditional averages over different numbers of events shows striking qualitative similarity with laboratory data, but the bursts occur at much longer time intervals (of the order of one per minute) than inner scaling would imply.

2.3. Flux events

A modification of the VITA technique, permitting detection of events directly from the instantaneous product of the fluctuating velocity components, has been applied to analyse momentum flux events. It is found that events detected at low t_{av} (say 0.3s) tend frequently to form 'clusters', which appear as single events at larger t_{av} (e.g., 10s). Such events are termed 'super-events'. Other events which stand isolated at any t_{av} are termed 'ordinary events'. Ordinary events are again found to be of two types, those that are detected only at some particular t_{av} (called 'uncorrelated ordinary events') and others detected over a wide range of t_{av} (called 'correlated ordinary events').

Analysis of stress generation rates shows that each super-event contributes on an average twice as much to the total flux as an ordinary event.

Conditional averages of flux events reveal encouraging similarity with those measured in the laboratory (e.g. Thomas¹³). The flux-generation profile of each event reveals two distinct regions. In the 'core' of the event (within $\pm 10s$ of the centre), the stress generation rate is of the order of 10^{-16} of the total flux per second. In the 'wings', on the other hand, the rate is an order of magnitude lower.

2.4. Probability distribution of event intervals

The distribution of the time intervals between events (i.e., time from the centre of one event to the next) shows that at $t_{av} = 0.3s$ the distribution is skewed towards its ends with more than half the events being located closer than 20s to the next, while the longest event interval is much larger ($> 100s$). On the other hand, the distribution at $t_{av} = 10s$ is weighted more to the centre of the range with more than half the intervals occurring between 30 and 70s, the largest interval being less than 80s. These distributions are similar to results on the time interval between ejections from the same streak and from different streaks reported by Bogard and Tiederman⁶ in a laboratory study of channel flow. However, there is a difference of orders of magnitude in the number of events detected per unit time, and hence in the mean interval between these events. Bogard and Tiederman⁶ have differentiated a burst from an ejection, and proposed that the modified VITA technique applied to the present flux signal and filtered at $t_{av} = 10s$ detects a burst in this sense, i.e., a whole organized cycle of ejections.

2.5. Flux contribution from the biggest events

The complete event may be delimited by the points of intersection of the stress generation curves from neighbouring events. The contribution to the flux from each event may then be determined, and the events ordered in size starting from the biggest contributor. It is found that around 11 ± 2 events in each 12-minute stretch account for over 90% of the flux in around 75% of the time. Thus the number of the most significant (i.e., flux-generating) events is of the order of 10 in a 12-minute stretch.

2.6. Measurement of burstiness

From the above computations, a curve can be drawn showing the cumulative flux contribution against cumulative duration for events ordered downwards according to intensity. A strictly linear increase in flux contribution with time would indicate that flux generation is distributed evenly in time. The area covered by the departure of the observational curve from linearity, suitably normalized, is proposed here as a measure of 'burstiness' B . With the normalization adopted $B = 0$ if the contribution is evenly distributed in time and takes a maximum value of unity if the total duration of all events is zero, i.e., they are all 'instantaneous'. Thus burstiness quantifies both the compactness and intensity of events detected in a flow. The maximum value of B in all stretches analysed here was around 0.5 over heights ranging from 10 to 300 m above ground, remaining nearly independent of the threshold k over a range of 0.1 to 1. Clearly, the events detected by the modified VITA technique contribute to the total flux at rates well above the average.

3. Conclusions

1. The VITA technique reveals the existence of energy events in the atmosphere which are remarkably similar in structure to those previously detected in low Reynolds number laboratory flow studies. However, atmospheric events occur at a frequency of the order of one per minute, which is much lower than inner scaling would imply and is not inconsistent with outer scaling.
2. A modification of the VITA technique proposed here, when applied to the flux signal, reveals events with many similarities to those detected in the laboratory, e.g., in the conditionally averaged velocity and flux profiles, and their dependence on the height from the boundary. Several new features of flux event profiles are reported.
3. The modified VITA at an appropriate t_{av} automatically detects a special class of what we term here as 'super-events'.
4. The 'core' region of flux events, identified from the associated high rate of stress generation, contributes to the stress at rates an order of magnitude higher than the 'wings' of the event.
5. Around ten events in a 12-minute stretch account for about 90% of the total flux.
6. A measure of the burstiness of the events described here is proposed, and shown to be nearly independent of event intensity in the range $k = 0.1$ to 1. The burstiness in this range of k is found to be -35 ± 0.1 , and does not show any strong variation with height above ground.

References

1. KLINE, S. J., REYNOLDS, W. G., SCHRAUB, F. A., AND RUNSTADLER, P. W. *J. Fluid Mech.*, 1973, **30**, 741-773.
2. RAO, K. N., NARASIMHA, R. AND NARAYAN, M. A. B. *J. Fluid Mech.*, 1971, **48**, 339-352.
3. GRASS, A. J. *J. Fluid Mech.*, 1971, **50**, 223-255.
4. JOHANSSON, A. V AND ALFREDSSON, P. H. *J. Fluid Mech.*, 1982, **122**, 295-314.
5. RAJAGOPALAN, S. AND ANTONIA, R. A. *Phys. Fluids*, 1984, **27**, 1966-1975.
6. BOGARD, D. G. AND TIEDERMAN, W. G. *J. Fluid Mech.*, 1986, **162**, 389-413.
7. GORDON, C. M. *Nature*, 1974, **248**, 392-394.
8. GORDON, C. M. *Phys. Fluids*, 1975, **18**, 141-144.

9. HEATHERSHAW, A. D. *Nature*, 1974, **248**, 394-395
10. JACKSON, R. G. *J. Fluid Mech.*, 1976, **77**, 531-560.
11. BLACKWELDER, R. F AND KAPLAN, R. E. *J Fluid Mech* , 1976, **76**, 89-112
12. KAIMAL, J C AND GAYNOR, J E *J. Appl. Met.*, 1983, **22**, 863-880
13. THOMAS, A. S. W. *AGARD CP 271*, Paper 26, 1977.

Thesis Abstract (Ph.D.)

Some studies on the uplift and axial capacity of piles by K. H. Venkatesh.

Research supervisor: K. S. Subba Rao.

Department: Civil Engineering.

1. Introduction

Although piles are generally made in groups, the understanding of single pile-soil interaction becomes important as it still forms a major input in the design of pile foundations. Studies on the behaviour of piles^{1,2} have helped in identifying factors influencing the pile-soil response but many uncertainties and conflicting views still remain about their influence. In particular, the skin-friction behaviour with regard to the failure surface, and the stress-level dependency of the pile-soil interaction coefficients are aspects still not clearly understood. Further, for piles in clay, information regarding the adhesion factor α and its dependency on pile roughness and stress level is not available. To address all these issues an extensive experimental investigation was undertaken.

2. Experimental programme and methodology

Two series of model tests were conducted. In the first, pile testing was carried out in the conventional manner wherein soil is contained in a test tank and no surcharge pressures are imposed on the soil. A major drawback in the conventional method of testing is that the earth pressure coefficient, K_s , cannot be assessed from shaft load measurements without an input of $\tan \delta$. The pile-soil friction angle δ is usually assessed from direct shear tests which do not truly reflect the pile-soil interface characteristics consequently affecting the assessment of K_s . Because of this and other drawbacks an alternative testing methodology was developed resulting in the second series of tests. The testing methodology involves tests in two phases using a large triaxial chamber. In the first phase, σ_v tests under controlled vertical stresses are conducted for the determination of point resistance and so the bearing capacity factor N_q . In the second phase, σ_h tests under controlled horizontal stresses similar to the tests reported by Coyle and Sulaiman³ are conducted for the determination of point and shaft resistances.

Both push-in and pull-out tests on buried and driven piles in sand were conducted using 12.7 mm dia smooth and 13.4 mm dia rough piles at various length-to-diameter ratios (L/d) of between 6 and 20. A few tests on smooth piles of 19.05 mm dia driven into sand were also conducted. The relative density of sand was varied between 40 and 80%. Apart from tests in sand, push-in tests on buried piles in clay were also conducted to measure the tip and shaft resistances.

3. Uplift theory for bored piles in sand

It is now well established that the unit skin friction does not increase monotonically with pile depth but instead reaches almost constant values beyond a certain critical depth^{1,2}. At present an uplift theory which predicts such a behaviour is not available. A general theory for uplift of bored piles in sand having not only the capability of predicting the ultimate skin friction but also that of the critical depth beyond which skin friction becomes constant has been developed in this work. The theory is based on the assumption of a curved failure surface initiated along the pile shaft at the tip level and gradually progressing upwards and outwards until it is inclined at the ground level at $(45 - \phi/2)$ to the horizontal. The ultimate uplift

capacity in terms of the pile length, pile roughness and shear strength of soil has been arrived at by the limit equilibrium method. Comparison of the theory with the experimental results obtained from literature indicates that predictions made using the suggested theory are not only as good as those made using other available theories^{4,5} but also in accordance with the actual behaviour of piles in uplift. In other words, the theory is also capable of predicting very reasonable values of the extent of failure surface at the ground level and the limiting skin-friction and critical depth values.

4. Results and conclusions

Test results indicate that the developed testing methodology can afford satisfactory and realistic assessment of pile-soil interaction coefficients such as N_q , K_s and $\tan \delta$ for piles in sand, and N_c and α for piles in clay. From direct measurements of pile-soil friction angle δ through σ_h tests, it is found that δ varies from 18 to 20° for smooth piles depending on the relative density. For the rough piles, δ is greater than ϕ and depends on soil density and stress level to a little extent. This suggests that failure is not exactly along pile-soil interface but a little away from it. The extent of failure surface depends on the stress level in soil and pile length. For the limiting condition of $\delta = \phi$, the failure surface diameter is about 2.5 pile diameters for tests without surcharge, while for tests with surcharge it is 2 pile diameters.

By a combination of σ_v and σ_h tests, earth pressure coefficients have been assessed directly without consideration of $\tan \delta$. The procedure for assessment of K_s is to determine the σ_v and σ_h stress levels from the corresponding tests which give the same unit point resistance value for a given density of soil and pile type. The ratio σ_v/σ_h then automatically gives K_s . The average K_s values so determined vary from 0.84 to 1.4 and are not significantly affected either by ϕ or δ .

Push-in and pull-out tests indicate that the unit shaft resistance during pull-out is less than that during push-in by about 20% for buried piles and by as much as 50% for driven piles.

Stress level in the soil also affects the unit tip resistance and therefore the bearing capacity factors. For piles in medium dense sand N_q decreases from 300 to 51 at surcharge pressure of 0.64 kg/cm². Further, N_q reaches a constant value of about 19 at higher stress levels beyond 3 kg/cm². For piles in clay a constant N_c value of 9 is usually assumed for pile designs⁶. However, tests indicate that N_c varies from 7 to 12 depending on the stress level in the soil, higher the stress level higher being the value.

For piles in clay, the adhesion factors depend on soil shear strength, stress level and pile roughness. In this case too, shaft failure for rough piles is away from the pile-soil interface. The failure surface diameter is about 1.6 dia. The adhesion factor variation is from ~ 0.2 to ~ 0.94.

References

1. VESIC, A. S. Investigations of bearing capacity of piles in sand, *Proc. North Am. Conf. on Soil Mech. and Foundation Engng.*, Mexico, 1964, pp 197-224.
2. MEYERHOF, G. G. Bearing capacity and settlement of pile foundations, *J. Geotech. Engng Div., ASCE*, 1976, **102** (GT3), 195-228.
3. COYLE, H. M. AND SULAIMAN, I. H. Skin friction for steel piles in sand, *J. Soil Mech. Foundation Div., ASCE*, 1967, **93** (SM6), 261-278.
4. MEYERHOF, G. G. The uplift capacity of foundations under oblique loads, *Can. Geotech. J.*, 1973, **10**, 64-70.
5. CHATTOPADHYAY, B. C. AND PISE, P. J. Uplift capacity of piles in sand, *J. Geotech. Engng. ASCE*, 1986, **112** (GT9), 888-904.
6. POULOS, H. G. AND DAVIS, E. H. *Pile foundation analysis and design*, 1980, Wiley.

Thesis Abstract (Ph.D.)

Bearing capacity of reinforced soil beds by Hans Raj Singh.

Research supervisors: A. Sridharan and B. R. Srinivasa Murthy.

Department: Civil Engineering.

1. Introduction

Reinforced soil is one of the fast growing construction techniques which is becoming popular all over the world. One of the potential fields of application where this technique could be effective alternative to the conventional ground improvement techniques is in the improvement of bearing capacity of weak soils. Reinforced soil foundation bed is a soil foundation containing horizontally embedded thin flat metal strips, ties or grids.

Although the concept of reinforcing weak foundation soils is no new idea, it is yet to be exploited. To bring the study on reinforced soil bed to a stage at which it can be adopted for designs, appropriate analyses supported by suitable experiments are necessary. This investigation is an attempt towards this goal.

2. Scope of the present investigation

A critical review and discussion on the available literature point to the fact that more research work is needed to understand the behaviour of reinforced soil beds and to formulate suitable analysis and design methods for the same. It is in this direction the scope of the present work has been formulated. This involves evolving suitable methods of analysis for various types of footings, experimental verification of the methods and formulation of suitable design procedures. It is proposed to study the possibility of using the grid reinforcements with appropriate method of analysis. It is attempted to throw more light on the mobilization of friction coefficient.

3. Analysis of reinforced soil beds

The method of analysis developed by Binquet and Lee^{1,2} does not agree fully with the experimental observations due to a number of simplifying assumptions. In this investigation we propose modifications to the above method of analysis and extend the same to other shapes of footings, viz., rectangular, square and circular.

The overall analysis requires the estimation of normal force on the plan area of the reinforcement projected beyond the edges of the footing. Using elastic theory, solutions have been obtained, charts and tables have been presented which help in the ready estimation of normal force on a given configuration of the reinforcement. The bearing capacity problem has been solved at two stages, viz., load-carrying capacity at a given settlement and the ultimate load-carrying capacity. An approach to estimate the realistic value of mobilised angle of interfacial friction has been presented. The analysis on the bearing capacity has resulted in the development of general equations of the bearing capacity ratio for the above conditions. The overall examination of the resulting equations for bearing capacity ratio has been made in terms of variations of different and mutually dependent parameters like depth of first layer of reinforcement, vertical spacing between the reinforcement layers, length of reinforcement, number of layers and shape and size of the footings.

4. Experimental validation of the analysis

The validity of the above proposed method of analysis in relation to the results of carefully conducted model plate load tests is examined. The experimental programme essentially consists of a series of model plate load tests on dense sand reinforced with aluminium strips, varying the different parameters. A brief discussion on the mechanism of interfacial friction mobilisation and the method of determination of the same has been presented. An examination of the methods of analysis proposed has indicated its validity to a high degree for the cases of load settlement behaviour and ultimate failure conditions, in relation to the experimental data.

5. Alternative reinforcement form—The grids

The mobilisation of interfacial friction is essential for the performance of reinforced soil beds. It is attempted to achieve more effectively the mobilisation of interfacial friction by using alternative reinforcement pattern in the form of grids. This has been attempted through a systematic experimental programme consisting of plate load tests on reinforced soil beds with grids. The effect of various parameters, viz., depth of first layer, number of layers, size and placement pattern of the reinforcement, and size and shape of the footings on the load-settlement behaviour has been brought out.

6. Analysis of reinforced soil beds with grid reinforcement

The method of analysis which is presented for strip reinforcement is examined for grid reinforcement. The test results with grid reinforcement presented in this investigation form the basis. The behavioural mechanism and mechanism of mobilisation of interfacial friction has been brought out. Charts and tables for non-dimensional normal force factor applicable to grid reinforcement are presented. After certain modifications to the method of analysis proposed for strip reinforcement, it fully satisfied the results obtained with the grid reinforcement.

7. Design of reinforced soil beds

With the method of analysis developed for reinforced soil beds with aluminum strip/mild steel grid reinforcement for different shapes of footings and examination of their validity through the experimental results, it is possible to formulate a design methodology for reinforced soil beds. The design procedures are presented in this investigation with suitable examples.

8. Conclusions

The following specific conclusions of practical importance are made in this investigation.

The analysis presented by Biauquet and Lee for the case of strip footing with strip reinforcement needs some modifications to explain the experimental results consistently. Modifications were made to extend it to other shapes of footings and grid reinforcement.

The modified analysis of reinforced soil foundation beds has resulted in the development of unique equations for the bearing capacity ratio (which is defined as the ratio of load carried by the reinforced soil to that of the unreinforced condition at the same settlement level).

The computation of normal force on the plan area of reinforcement and estimation of the interfacial friction angle are the two essential steps in the computation of bearing capacity ratio. The process has been simplified by presenting suitable charts and tables in non-dimensional forms which can be directly used for the same purpose.

The proposed method of estimation of strain level at different positions of the reinforcement appears to be reasonable and using this the interfacial friction angle at different reinforcement position and settlement level can be obtained from the results of direct sliding or pull-out tests, as the case may be.

If strip reinforcement is not interconnected, such reinforcement which is parallel to the edges of the footing and placed beyond the edges, does not contribute to the load-carrying capacity and hence need not be used.

For a given type of reinforcement material, the thickness of the reinforcement will not influence much in the mobilization of interfacial friction.

The depth of first layer of reinforcement from the level of the footing, irrespective of the number of layers of reinforcement, appears to be optimal at 0.25B.

The optimal vertical spacing between the reinforcement layers depends on the total number of layers and size of the reinforcement.

Bearing capacity ratio is generally proportional to the number of layers up to four layers and further the rate of increase per layer decreases.

For grid type of reinforcement, bearing capacity ratio is proportional to the size of the reinforcement up to $2B \times 2B$ size and further the increase in bearing capacity ratio is not significant.

The shape effect of the footing is not pronounced in the case of reinforced soil due to coherent mass action of the reinforced soil. However, the bearing capacity ratio depends on the shape of the footing due to the dominance of the shape factor on the unreinforced condition.

The effect of size of the footing on reinforced sand bed is similar to that of unreinforced condition, the number of layers of reinforcement being the same.

In the analysis of reinforced soil beds with stiff grid reinforcement, the reinforcement present right below the footing plays an important role. Due to several contributing factors, it makes the footing to behave as if it has been located at the level of bottom-most layer of the reinforcement. The additional bearing capacity ratio obtained thus should be added to the predicted bearing capacity ratio.

References

1. BINQUET, J AND LEE, K L Bearing capacity tests on reinforced earth slabs, *J. Geotech. Engng Div*, *ASCE*, 1975, 101(GT-12), 1241-1255.
2. BINQUET, J. AND LEE, K. L. Bearing capacity analysis of reinforced earth slabs, *J. Geotech. Engng Div*, *ASCE*, 1975, 101(GT-12), 1257-1276

Thesis Abstract (Ph.D.)

Design for testability and fault analysis in PLAs and general combinational circuits by James Jacob.

Research supervisor: N. N. Biswas.

Department: Electrical Communication Engineering.

1. Introduction

With the advent of very large scale integrated (VLSI) circuit technology, the problem of test generation and fault diagnosis for these devices has become an extremely complex task. A single VLSI chip may today contain more than one million components and their interconnections. Development of algorithms that can efficiently generate test vectors for such complex digital logic circuits is an active area of current research. Further, design for testability (DFT) techniques, which aim to simplify the testing problem by incorporating additional circuitry, are gaining acceptance. Theoretical results on the multiple fault detection capability of single fault test sets are also useful since most test-generation algorithms make the simplifying assumption that only one fault is present in a circuit at a given instant.

This work makes three contributions to the area of digital logic testing. First, an efficient test-generation algorithm is developed and implemented in software for an important class of circuits known as programmable logic arrays (PLAs). Second, a DFT technique requiring minimal extra hardware, which makes the testing of PLAs extremely simple, is proposed. Third, a theoretical analysis of the multiple fault coverage capability of single stuck fault test sets is carried out, which brings out the necessity of test sets with high coverage of faults of relatively small sizes.

2. Test-generation algorithm for PLAs

PLAs are being extensively used in today's LSI and VLSI circuit design and are generally tested employing the crosspoint fault model. The four types of crosspoint faults that may occur in a PLA may be classified as growth, shrinkage, appearance and disappearance faults. An algorithm named PLATES is developed

to generate a near-minimal test set to detect all signal crosspoint faults in a PLA¹. Powerful heuristics are employed to speed up the test generation and minimization phases, both of which are known to be NP-complete problems. A novel feature of the algorithm is that for the large number of shrinkage faults in a PLA, time-consuming cubical set difference computations have been completely avoided. It is proved that shrinkage tests can be derived from the set of disappearance tests on a product term by adopting a simple fault-simulation strategy along with cubical intersection operations. The performance of a Pascal implementation of PLATES is compared with that of PLATYPUS, which is the best known PLA test-generation algorithm currently available. It is shown that PLATES has a run-time performance similar to PLATYPUS and on the whole leads to over 7% savings in the size of the test set.

3. Design for testability

The need to design PLAs for testability is highlighted by pointing out the deficiencies of test sets derived under the single crosspoint fault assumption². A simple scheme to design a completely testable PLA by adding a shift register and an extra observable output line called watch-line is developed. This approach highly simplifies the test generation for PLAs and ensures the detection of all possible combinations of multiple crosspoint, stuck and bridging faults. The proposed design requires less extra hardware and fewer test vectors compared to other competing approaches and also adds an online checking feature to the testable PLA³.

4. Multiple fault coverage analysis

An analysis of the multiple stuck fault detection capability of a single fault test set (SFT) is carried out for general multiple-output combinational circuits⁴. Certain faults in a circuit are guaranteed to be detected (GTBD) by any SFT for all single-stuck faults in the circuit, irrespective of the presence of other faults. A formula to compute the fraction of GTBD faults in a circuit is derived. This leads to a simple method of obtaining a lower bound on the multiple fault coverage of any SFT for the circuit. It is seen that the fraction of GTBD faults in any circuit rises exponentially with the number of observable outputs and the number of fan-in lines to the output gates. A rather unexpected result borne out by the above analysis is that at least 99.6% of all multiple faults are GTBD in any combinational circuit with three or more observable outputs.

A more detailed analysis is done to determine the contribution of GTBD faults of specific multiplicities to the overall multiple fault coverage of an SFT for the circuit. It is shown that irrespective of circuit structure, the fraction of GTBD faults in a circuit rises exponentially as the fault size increases. It is clearly established that the very high overall multiple fault coverage of SFTs observed in most practical circuits is mainly due to the increasingly large fraction of GTBD faults at higher fault sizes. The analysis provides a theoretical justification to the popular view that a test set having a high coverage of faults of relatively small multiplicities is both necessary and sufficient to detect all multiple stuck faults of interest in the circuit.

5. Conclusion

It is hoped that the results reported in this work will find practical application in the testing and DFT of PLAs and stimulate further research in the analysis of multiple fault coverage by SFTs under different fault models.

References

1. JAMES JACOB AND BISWAS, N. N. PLATES: An efficient PLA test pattern generator, *Proc. Third Int. Workshop on VLSI Design*, Bangalore, India, Jan. 1990, pp 147-154.
2. JAMES JACOB AND BISWAS, N. N. Further comments on detection of faults in programmable logic arrays, *IEEE Trans.*, 1990, C-39, 155-156.
3. BISWAS, N. N. AND JAMES JACOB A testable PLA design with minimal hardware and test set, *Proc. IEEE Int. Test Conf.*, Philadelphia, USA, November 1985, pp 583-588.

4. JAMES JACOB AND BISWAS, N. N.

GTBD faults and lower bounds on multiple fault coverage of single fault test sets, *Proc. IEEE Int. Test Conf.*, Washington, USA, September 1987, pp 849-855.

Thesis Abstract (Ph.D.)

Diagnostic reasoning using surface and deep level knowledge in medical domain by S. V. R. K. Prabhakar.

Research supervisors: I. S. N. Murthy and L. M. Patnaik.

Department: Electrical Engineering.

1. Introduction

Diagnostic reasoning for real-world domains is a computationally complex problem. The necessity for the intermediate steps generated by the problem solver to match with those of the expert reasoner adds to the complexity problem. This problem has been addressed in several expert systems by organizing their knowledge around a model. But, in natural systems like human body, simple or single models may not be often adequate. In this work, we propose multiple/complex models to organize and use diagnostic knowledge.

2. Conceptual development

The models we propose have three different characteristics: (i) task specificity, (ii) multiple or complex models, and (iii) choice of model depending upon the level of knowledge used for diagnosis. Two expert systems, one each for surface- and deep-level knowledge, have been developed.

3. Diagnosis with surface-level knowledge

In this case, large number of heuristics needs to be used. Several systems^{1,2} have proposed an organization of this surface-level associational knowledge around a taxonomy. But, often the diagnostic knowledge of real-world domains is incomplete and cannot be organized into a single taxonomy.

We organize the knowledge into multiple taxonomies. Further, each taxonomy represents an organization around a feature — structures, faulty state, or cause of fault. The domain is partitioned into well-structured islands where this taxonomic organization is possible.

Each node in the taxonomy stands for a disease category and captures a variety of heuristics. The situational heuristics draw conclusions in three situations — typical, atypical and multiple diagnoses. One of the control heuristics directs reasoning within a taxonomy, either by generalizing or specializing a category. The other types of control knowledge navigate reasoning from one taxonomy to other taxonomies.

Diagnosis is finding the structural location of fault, the disease state of that location and the cause. All the taxonomies cooperate to arrive at these aspects of diagnosis. This happens due to the local decisions taken within the taxonomies.

These ideas have been implemented in a system called INTERX in ELISP on a DEC-1090 system. The domain of illustration was infectious diseases.

4. Deep-level knowledge for diagnosis

For rare and difficult cases, deep-level knowledge needs to be used. Several systems^{3,4} have used deep-level knowledge to diagnose a fault arising in a physical system. But in human body several faults can arise independently. Qualitative simulation (QS)³ is very useful for generating abnormal behaviour of a physical/conceptual system. But applying QS for multiple faults case leads to computational complexity.

We have developed a fault-oriented process language. These processes include lesion change, exudation, cellular change and transportation. This causal knowledge is organized around an environment and an enclosed system where the latter has more detailed causal knowledge of faults. These ideas are illustrated for the domain of respiratory tract, infectious diseases.

A new level of hypothesis has been identified—a disturbance in the environment called root cause. In the domain of illustration, it is an external organism. When it enters the body, it can cause multiple faults. The causal knowledge is organized around a taxonomy where each node represents the entry of a root cause into the physical system.

These ideas have been implemented in a system called DIAN in ELISP on a DEC-1090 system. The DIAN system, implemented for the respiratory tract infectious diseases, has 6 root causes, 209 enclosed and 50 environmental system processes and 80 manifestations. The control structure has a hierarchy of 23 operators organized into five layers.

5. Conclusions

In this work, several new ideas have been developed about knowledge organization and representation by observing some common intuitions the physicians exhibit. The organizations and concepts have addressed to the computational complexity problem which is acute in difficult diagnostic problems in the real-world domains. Two expert systems developed show an improved performance over the structured systems.

References

- GOMES, F. AND CHANDRASEKARAN, B. Knowledge organization and distribution for medical diagnosis, in *Readings in medical artificial intelligence*, W. J. Clancey and E. H. Shortliffe (eds), 1984, Addison-Wesley.
- AIKINS, J. S. Prototypical knowledge for expert systems, *Artif. Intell.*, 1983, **20**, 163-210
- DAVIS, R. *Diagnostic reasoning based on structure and behavior*, AI Memo 739, AI Lab., MIT, June 1984.
- PAN, Y. C. *Qualitative reasoning with deep-level mechanism models for diagnosis of dependent failures*, AI Tech. Report, No. 38, Palo Alto Research Center, Shlumberger, 1984
- BOBROW, D. G. *Qualitative reasoning about physical systems*, 1985, MIT Press.

Thesis Abstract (Ph.D.)

Experimental study of a small turbine with partial admission by A. K. Varma.

Research supervisors: S. Soundranayagam and F. M. Soonawalla (HAL).

Department: Mechanical Engineering.

1. Introduction

Small turbines are extensively used amongst other things in power packs to drop the enthalpy of gases in liquefaction plant and as expanders in air-cooling plant. Their design techniques however have not been as firmly established as that of larger turbines. This work deals with the design and experimental analysis of a small turbine expander for the cockpit cooling system of a fighter aircraft. The design is that of a small partial admission unit of extreme geometry, rather than a conventional radial turbine, to explore the uncertainties in the design and performance of such units.

The design specifications called for a cooling load of 2.5 kW utilising air bled from the engine compressor.

The turbine specifications were,

Total inlet pressure	: 517×10^3 Pa (75 psia)
Total outlet pressure	: 128×10^3 Pa (18.5 psia)
Total inlet temperature	: 353 K
Mass flow	: 5.2 kg/min (11.5 lb/min)
RPM	: 44,300

The resultant impeller had an overall diameter of 80.3 mm (3.16") with a blade height of 3.66 mm (0.14") and partial admission of 60 per cent.

2. Experimental programme

Measurements were carried out in a specially constructed test rig, efficiencies being derived from careful measurement of pressure and temperature. Techniques were developed to allow the effect of humidity in the inlet flow. Tests were carried out at full admission and the design admission ratio opened out into two and three sectors. The turbine was loaded by driving a centrifugal fan, the load being varied by throttling the fan at outlet.

3. Results and discussion

Contrary to the usual expectation, there was considerable build up of pressure in the gap between the rotor and stator for partial admission, the pressure increasing with the blade speed ratio. The increase with blade speed was present even with full admission.

The measured efficiency was much lower than originally anticipated in the design. The experimental variation of efficiency was fairly closely predicted (Fig. 1) using the correlations of Ainley and Mathieson¹ suitably corrected to allow for aspect ratio² and disc friction. The updated correlations of Craig and Cox³ could not be used successfully due to uncertainties at large flow angles.

The effect of partial admission on efficiency is seen in Fig. 2 where the efficiency debit increases rapidly above the optimum blade speed ratio. The attempt to predict the variation of efficiency at partial admission is fairly successful at the optimum blade speed ratio but is unable to reproduce the rapid fall in efficiency at higher speed ratios (Fig. 3). A theoretical expression developed for the effect of multiple sectors of admission developed for the effect of multiple sectors of admission on the optimum blade speed ratio shows that the latter reduces with increase in the number of sectors as is reflected in the experimental results.

The biggest loss by far is that due to secondary flow and is particularly severe at the very low aspect ratios used in the present design. It is important to include disc-friction losses in such turbines in the prediction of efficiency. While the trend of off-design efficiency variation is reasonably good under full admission conditions, much more detailed information is necessary on the off-design losses in partial admission turbines if the performance over the whole operating range is to be realistically predicted.

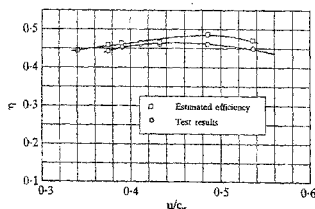


FIG. 1 Comparison of predicted and experimental variation of efficiency.

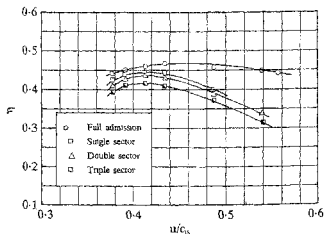


FIG. 2 Variation of efficiency with partial admission.

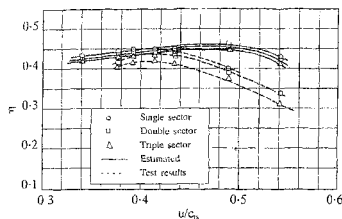


FIG. 3 Prediction of efficiency at partial admission

References

- AINLEY, D. G. AND MATHIESON, G. C. R. *An examination of flow and pressure losses in blade rows of axial turbines*, NGTE, R+M No. 2891, 1951.
- KACKER, S. C. AND OKAPU, U. *A mean line prediction method for axial flow turbine efficiency*, ASME 81-GT-58, 1981.
- GAG, H. R. M. AND COX, H. J. A. *Performance estimation of axial flow turbines*, *Proc. Instn Mech. Engrs*, 1970-1971, **185**-32/71, 407-424.

Thesis Abstract (Ph.D.)

Studies on cavitation inception process in separated flows by S. George Milton.

Research supervisor: Vijay H. Arakeri.

Department: Mechanical Engineering.

1. Introduction

The present work is aimed at gaining a better understanding of the cavitation inception process in separated flows. It is well known that the viscous flow around a body does significantly affect the inception characteristics of the body. For example, on a hemispherical-nosed body, the inception does not take place in the region of minimum pressure, but somewhere downstream in the region where the shear layer reattaches after separation. The role of the laminar-separated regions appears very striking in the sense that the same liquid sample in the free stream which readily cavitates in the presence of a separated region is able to withstand tensions in the absence of separation region, deliberately removed¹. Furthermore, experiments showed that inception on the bodies possessing laminar separation is relatively insensitive to the variations in nuclei content in the free stream². Nuclei population measurements in the separated region and in other sections of flow showed that appearance of visible cavitation was preceded by the appearance of cluster of microbubbles in the separation region while the nuclei population remained uniform elsewhere. It can be conjectured from the above observations that nuclei once entrained in the separated region may be growing by gaseous diffusion, thus altering the nuclei population locally. Since a nucleus once trapped in the separated region is likely to be subjected to unsteady pressure field, there is a distinct possibility for the nucleus to grow by rectified diffusion or turbulent diffusion apart from static diffusion.

One of the aims of the present work is to experimentally investigate if any of the above-mentioned diffusion processes can be an important mode of nuclei growth in separated regions. At the outset it became clear that this issue could not be resolved by studying or observing bubble growth patterns in

naturally separated regions since in this case the nuclei are subjected to both steady and unsteady pressure fields. Therefore, an experimental configuration had to be thought of where some of the properties of the separated regions like long residence time of nuclei are simulated, at the same time having the possibility of subjecting the trapped liquid sample to the desired pressure field. It was felt that this could be achieved by trapping a liquid sample in a groove placed on an axisymmetric body with its axial location suitably selected.

2. Experimental methods

Experiments were conducted in the High Speed Water Tunnel at the Indian Institute of Science, Bangalore. Axisymmetric grooves were placed at different axial locations on different models, all having a 1.5 caliber ogive for their nose profile. The groove locations were such that the boundary layer is either only laminar, transitional or turbulent for the tunnel velocity range employed in the present studies. The selection of the groove locations was based on Schlieren flow visualisation. Pressures at which the bubbles appeared (*i.e.*, inception) in the grooves were recorded. Such studies were carried out under natural conditions and also in the presence of artificially created pressure fluctuations. One of the grooves with laminar boundary layer above it was subjected to pressure fluctuations created by a hydrophone axisymmetrically placed inside the model and inception pressures were recorded for that groove. The time nuclei spend in the grooves is an important factor in deciding the size to which they grow. In view of this fact a technique to measure the residence time of the nuclei was developed with a view to getting an order of magnitude values. In addition to the above, spectra of fluctuating pressure were obtained for two groove locations, one with transition occurring above it and the other with turbulent boundary layer. Fluctuating pressure measurements were also made under tripped boundary layer conditions.

3. Results and discussion

From Schlieren flow visualization studies it was found that for groove location at $x/D = 1.136$ the boundary layer was laminar and for $x/D = 1.206$ it was transitional for the tunnel velocity range employed. For groove at $x/D = 0.47$ the boundary layer was laminar and for $x/D = 1.5$ it was expected to be turbulent for the employed tunnel velocity range. Inception tests conducted clearly showed that inception occurred at higher pressures in the 'turbulent' groove ($x/D = 1.5$) compared to the 'laminar' groove ($x/D = 0.47$). The results in the form of non-dimensional cavitation number *versus* tunnel velocity are shown plotted in Fig. 1. No definite conclusions could be made for inception in the 'transition' groove ($x/D = 1.206$). It appears that the growth of bubbles in the grooves is due to gaseous diffusion and among the various forms of diffusion possible, namely, static, rectified and turbulent diffusion, the last, *i.e.*, turbulent diffusion is more effective in enhancing the bubble growth rates. Residence time measurements indicated that residence time of the nuclei in the grooves is small being of the order of a few milliseconds.

4. Modelling

Assuming that the state of affairs in naturally separated regions is similar to what has been observed in the grooves, modelling of cavitation inception on hemispherical-nosed body was carried out for what is known as 'bubble-ring' cavitation. A typical nucleus as it travels along the surface of the body first encounters the low pressures upstream of separation where it may grow either vaporously or just experience an isothermal volume change. This is the first phase of growth. After this it is assumed to get entrained in the separation region where it undergoes gaseous growth by turbulent diffusion for a time determined by the residence time characteristic to the separation region. This is the second phase. At the end of this phase the bubbles will get entrained in the eddies in the turbulent transition region downstream where they will grow vaporously and collapse under the influence of pressure fluctuations. This is the third phase. Bubble dynamics equation which governs the vaporous growth of a bubble has been solved along with the relevant pressure history for the first and the third phases of growth. Turbulent diffusion growth of the bubble in the second phase was based on the surface renewal theories. The coupled equations were iteratively solved to get cavitation inception numbers. It was found that considerable difference exists between the predicted inception numbers for the cases with and without inclusion of turbulent diffusion; in the absence of the growth of the nuclei by turbulent diffusion the low pressure upstream of separation dominated inception. It could be demonstrated from the theoretical results that inception numbers are less

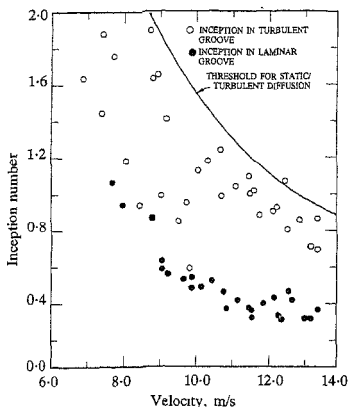


Fig. 1. Inception results for the grooves on the 75-mm turbulent groove model.

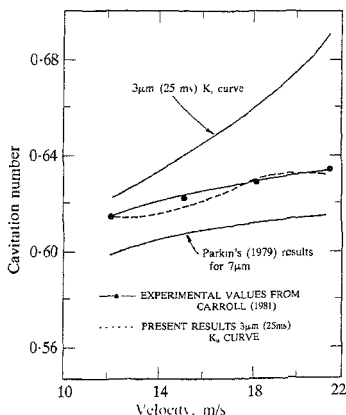


Fig. 2. Comparison of present results with experimental and Parkin's³ results

sensitive to change in nuclei size with the inclusion of turbulent diffusion than without it. Appropriate threshold values for unlimited vaporous growth in the third phase were obtained and it was found that Parkin's cavitation cut-off can take place even with the inclusion of turbulent diffusion³. The predicted inception numbers were compared with the experimental values and with Parkin's results as shown in Fig. 2. The agreement with experimental results for the cases of limited growth and unlimited growth is found to be satisfactory.

References

1. ARAKERI, V. H. AND ACOSTA, A. J. Cavitation inception observations on axisymmetric bodies at supercritical Reynolds numbers, *J. Ship Res.*, SNAME, 1976, 20, 40-50.
2. GATES, E. M. AND ACOSTA, A. J. Some effects of several free stream factors on cavitation inception on axisymmetric bodies, *12th Symp. Naval Hydrodynamics*, Washington DC, 1978.
3. PARKIN, B. R. *A theory of cavitation in the flow having laminar separation*, TM 79-198, ARL, Pennsylvania State University, 1979.

Thesis Abstract (Ph.D.)

Solid state galvanic sensors—some studies on concepts and materials by R. Akila.

Research supervisors: K. T. Jacob and A. K. Shukla.

Department: Metallurgy (under the interdisciplinary programme of Material Science).

1. Introduction

Solid-state galvanic sensors are useful for measuring the concentration of gaseous species in process streams and exhaust gases of a variety of high-temperature reactors. Sensors for oxygen have been used in the

laboratory and industry for a number of years. Sensors for SO_x ($x = 2, 3$) have gained importance with the awareness of the hazards of air pollution. Several materials, notably sulfates of alkali metals¹, with and without doping, have been used. However, each of the alkali sulfates undergoes a phase transformation to the high-temperature-conducting phase. The volume change accompanying the phase transformation can cause microcracking in sintered solid electrolyte pellets during temperature cycling and affect sensor performance over prolonged use. It would be fruitful to design sensors for SO_2/SO_3 using other solid electrolytes

In the case of sensors for S_2 and H_2S , some materials and designs have been identified and are under trial for industrial application. However, there is a need for better solid electrolytes, preferably sulfur ion conducting, for use in sulfur sensors. Rare-earth oxysulfides is one group of materials that show promise. Thermodynamic data on the stability of these oxysulfide phases are limited. The thermodynamic stability window is an important criterion in assessing a potential oxysulfide electrolyte for use in a sulfur probe.

Other areas of relevance to solid-state galvanic sensors studied include techniques to enhance ionic conduction at lower temperatures and the introduction of a new concept to measure the ability of an electrode system to accommodate small fluxes of a species without significantly altering the chemical potential of the particular species in the system.

2. Experimental results and conclusions

The performance of sensors for SO_x ($x = 2, 3$) species using β -alumina and NASICON solid electrolytes was studied using the cell arrangement



The open circuit emf across the cell was measured as a function of temperature for different gas compositions used. The measured emf agreed well with the value predicted by the Nernst equation for the sensor at all temperatures and gas compositions investigated. The intrinsic response time of the sensor to a step change in gas composition at the test electrode was measured at different temperatures for the two sensors. For the sensor employing β -alumina/ Na_2SO_4 couple, the intrinsic response time was in the range of ~ 1.9 ks at 750 K to ~ 0.06 ks at 1100 K. The sensor using NASICON/ Na_2SO_4 couple had an intrinsic response time ranging from ~ 2.0 ks at 723 K to ~ 0.2 ks at 1077 K. The solid electrolyte/ Na_2SO_4 couple used in the cell design protects the solid electrolyte from direct attack by SO_x species. Sodium sulfate is a known sodium ion conductor. It serves as an auxiliary electrode, converting the chemical potential of SO_3 and O_2 at the electrodes to an equivalent sodium potential which is measured by the solid electrolyte. The cell is mechanically stable over temperature cycling and chemically stable against attack by SO_3/SO_2 species.

Conductivity enhancement by doping with a second phase (heterogeneous doping) is a method of interest². Studies on conductivity enhancement by heterogeneous doping were performed using calcium fluoride as the model solid electrolyte. The second phase dopants used were Al_2O_3 and CeO_{2-x} . Conductivity measurements were performed under argon atmosphere at fixed frequencies of 1–2 kHz in the temperature range 630–1030 K. The ionic nature of conduction in the heterogeneously doped samples was verified by emf studies using metal + metal fluoride electrodes. At 630 K, the ionic conductivity of single-crystal CaF_2 increased by two orders of magnitude by doping with 2 mol% Al_2O_3 and by three orders of magnitude by doping with 2 or 4 mol% CeO_{2-x} . An insight into the mechanism involved in heterogeneous doping may be obtained by a novel method of combined homo-hetero doping which was experimentally studied. The homogeneous dopants used were YF_3 and NaF , while CeO_{2-x} was used as the heterogeneous dopant. The conductivity of CaF_2 containing both NaF and CeO_{2-x} was higher than that obtained using either dopant of the same composition alone. The effect was opposite when YF_3 was used as the homogeneous dopant. The total enhancement in conductivity of CaF_2 containing 0.5 mol% NaF and 2 mol% CeO_{2-x} was by 4.5 orders of magnitude at 630 K relative to pure, polycrystalline CaF_2 . A qualitative picture of the mechanism involved in heterogeneous doping was obtained from the combined doping studies. Auxiliary experiments using single-crystal CaF_2 confirmed that pure fluorine ion conduction prevails in CaF_2 , contrary to an earlier suggestion in the literature that CaF_2 is a mixed anionic conductor for fluorine and oxygen ions. The response of CaF_2 to an oxygen chemical potential gradient is through an exchange reaction involving the formation of CaO at the electrolyte/electrode interface.

Thermodynamic stability limits of rare-earth oxysulfides, R_2O_2S , where $R = La-Tm$, were determined as a function of temperature by a galvanic cell technique. Using an oxygen ion-conducting solid electrolyte with a suitable metal + metal oxide reference electrode, the equilibrium oxygen partial pressures for the coexistence of R_2O_2S and $R_2O_3SO_4$, R_2O_2S and R_2O_3 and R_2O_2S and R_2S_3 were measured as a function of temperature in the range 900–1300 K. The chemical potential of sulfur for the two-phase equilibrium of R_2O_2S and R_2O_3 or R_2O_2S and R_2S_3 was established by a buffer electrode mixture of a metal and its sulfide. The buffer electrode was physically separated from the rare-earth electrode to avoid errors arising from solid solubility or chemical reaction between them. The standard free energy changes calculated from the emf measurements were combined with available thermodynamic data on the rare-earth oxides (R_2O_3)³ to obtain standard free energies of formation of the rare-earth oxysulfides, oxysulfates and sesquisulfides as a function of temperature. The results represent the most comprehensive high-temperature thermodynamic data available on these rare-earth compounds. For a given temperature and chemical potential of sulfur, the results obtained can be used to determine the range of oxygen chemical potentials over which the rare-earth oxysulfides are thermodynamically stable. For example, at 1100 K and a sulfur partial pressure of 1 Pa, La_2O_2S is stable in the range of oxygen pressures from 10^{-6} to 10^{-15} Pa. The phases, La_2O_2S and $La_2O_2SO_4$, coexist at $p_{O_2} = 5 \times 10^{-9}$ Pa. Similar limits for the thermodynamic stabilities of the other rare-earth oxysulfides can be obtained. Thus the use of rare-earth oxysulfides in sensors for sulfur would be limited to atmospheres of low-oxygen chemical potential.

The constancy of the chemical potential of a species maintained by a reference electrode is a crucial factor in sensors. A change in the predefined chemical potential may result from a flux of species into the electrode system, arising from physical permeability or electrochemical semipermeability of the solid electrolyte. A new concept, thermodynamic capacity, has been introduced in this work. The newly defined variable provides a measure of the buffer capacity of the electrode system to maintain a desired value for the chemical potential of a species despite a small addition or removal of that species from the system. The thermodynamic capacity, C_i , of a species i can be mathematically expressed by the relation

$$C_i = (\delta n_i / \delta \mu_i)_{T,P,n_j} \quad (j \neq i)$$

Here n_i is the number of moles of species i irrespective of the chemical combination and μ_i is its chemical potential. The thermodynamic capacity may be visualised as the change in the number of moles of species i produced by a corresponding change in the chemical potential of i . The thermodynamic capacity of oxygen in various gaseous and condensed phases was calculated. For an optimum composition of the electrode system, the thermodynamic capacity of oxygen shows a maximum.

References

- JACOB, K. T. AND RAO, D. B. A solid state probe for SO_2/SO_3 based on Na_2SO_4 -I electrolyte, *J. Electrochem. Soc.*, 1979, **126**, 1842-1847
- MAIER, J. Space-charge regions in solid two-phase systems and their conduction contribution-I. Conductance enhancement in the system ionic conductor - 'inert' phase and application on $AgCl: Al_2O_3$ and $AgCl: SiO_2$, *J. Phys. Chem. Solids*, 1985, **46**, 309-320.
- GSCHNEIDNER, K. A. JR., KIPPENHAM, N. AND MCMASTERS, O. D. *Thermochemistry of rare earths*, Report No IS-RIC-6, Rare Earth Information Centre, Ames, Iowa, 1973, pp 5-37.

Thesis Abstract (Ph.D.)

Electron microscopic study of precipitation in an Al-Ge alloy—Analysis using near-CSL/DSC lattice model by Gouthama.

Research supervisor: Kishore.

Department: Metallurgy.

1. Introduction

Precipitation hardenable Al-Ge alloy system is believed to show a simple decomposition and sequence: Super-saturated $\alpha \rightarrow \alpha' +$ elemental Ge. A variety of precipitate morphologies, viz., rods, laths, triangular,

hexagonal, rectangular and square plates, with differing orientation relationships result during precipitation. In spite of large volume change of 36% involved in the precipitation of Ge in the Al matrix, the Ge precipitates form homogeneously. These unique characteristics make Al-Ge an important and interesting alloy system to study.

The aim of the present study is (i) to investigate the initial stages of decomposition; (ii) to identify the exact role of quenched-in excess vacancies in the nucleation and growth of Ge precipitates; (iii) to find the rationale behind the variety of orientation relationships and the corresponding precipitate morphology; (iv) to obtain detailed information about the characteristic features of the interphase interfaces; and (v) to compare the experimental results with the theoretical predictions of geometric models.

2. Experimental procedure

The alloy used in the present study is obtained by melting super-purity aluminium and 99.999% germanium and the composition is analysed to be Al-1.98 wt% Ge (0.72at. % Ge). The homogenised ingot is rolled in several stages with intermittent annealing at 400°C to obtain samples measuring $15 \times 15 \times 2$ mm which are subjected to the required heat treatment. The solutionising temperature ranged from 460 to 560°C. The treated samples are electrolytically thinned to electron transparency and studied using Philips EM301 transmission electron microscope.

3. Results and discussion

The as-quenched structure, obtained by quenching from 500–560°C into either water or oil at room temperature, produces circular loop-like features. A detailed investigation is undertaken to fully characterise the loop features in terms of their habit plane, Burgers vector and vacancy or interstitial character. Using the 'g·b = 0 invisibility' criteria all the loops are found to have $b = a/2(110)$. Based on trace analysis, the habit plane of majority of the loops is determined to be nearly {110} matrix and hence the loops are of edge character. Cases of shear loops with {111} habit are also identified. Using the FS/RH convention for defining, the Burgers vector and edge loops are found to be vacancy type while the shear loop turned out to be of interstitial type.

An atomistic model for the co-precipitation of super-saturated Ge atoms and quenched-in excess vacancies is developed which correctly explains the nature of loops. It is explicitly shown how layers of vacancy enter into the process of GP zone formation to relax the transformation strain. The dislocation surrounding the GP zone makes the first stage of nucleation in Al-Ge semi-coherent. The effect of pre-aging treatment in refining the precipitate distribution and results of *in-situ* experiments can be consistently explained by considering the zone size and stability as a function of aging temperature. Reviewing the experimental results of earlier investigators using other techniques on the system, it is shown here that the acceptance of GP zone formation can give more consistent interpretations. The non-observation of anomalous resistivity is taken to indicate that the zones are already formed at the end of the quenching process. The positron life-time values measured on the as-quenched Al-1.0 at.% Ge sample¹ being equal to typical values for dislocations are taken as another evidence strongly supporting semi-coherent GP zone formation.

The large volume change of 36% involved in the precipitation of Ge in Al matrix led earlier workers to believe that the Ge precipitates are incoherent from the beginning. Thermodynamic conditions prohibit homogeneous nucleation of such a phase at reasonable super saturations. But, experimentally homogeneous precipitation occurred in all specimens given a short pre-aging treatment at low temperatures. To explain this seemingly anomalous result, the theory of vacancy-aided homogeneous incoherent nucleation was proposed². The present study removes this anomaly by successfully identifying the GP zone stage.

The concept of coherency has undergone considerable refinement in recent years, and it has been shown that the state of coherency of an interface is a function of the lattice correspondence chosen³. Applying these concepts to precipitation systems, a coherent precipitate is considered to be the one for which all lattice sites are conserved. The possibility of such coherent three-dimensional precipitate is shown with the help of atomistic models with the identification of suitable lattice correspondence and

Table I
Shape and orientation relationship of germanium precipitates in aluminium-germanium

Shape	Orientation relationship	Habit plane	References
Triangular plates	(i) $(111)\text{Al} \parallel (111)\text{Ge}; [110]\text{Al} \parallel [110]\text{Ge}$	$\{111\}\text{Al}$ bounded by $\langle 110 \rangle\text{Al}$	Sorokin <i>et al</i> ⁵
	(ii) $(111)\text{Al} \parallel (111)\text{Ge}; [110]\text{Al} \parallel [211]\text{Ge}$	$\{111\}\text{Al}$	Present work
	(iii) $(011)\text{Al} \parallel (112)\text{Ge}; (100)\text{Al} \parallel (100)\text{Ge}$	$\{100\}\text{Al}$	Present work
Needle/Lath-shaped particles	(i) $(001)\text{Al} \parallel (111)\text{Ge}; [010]\text{Al} \parallel [011]\text{Ge}$	rods along $\langle 100 \rangle\text{Al}$	Köster ⁶
	(ii) $\{100\}\text{Al} \parallel \{100\}\text{Ge}; (100)\text{Al} \parallel (110)$		Dahmen and Westmacott ⁷
	(iii) $\{110\}\text{Al} \parallel \{110\}\text{Ge}; (100)\text{Al} \parallel (110)\text{Ge}$		
Rectangular plates	$(001)\text{Al} \parallel (111)\text{Ge}; [110]\text{Al} \parallel [110]\text{Ge}$	$\{100\}\text{Al}$ bounded by $\langle 011 \rangle\text{Al}$	Köster ⁶
Square plates	$(100)\text{Al} \parallel (100)\text{Ge}; [010]\text{Al} \parallel [011]\text{Ge}$	$\{100\}\text{Al}$	Present work
Tetrahedra	$[110]\text{Al} \parallel [110]\text{Ge}$		Hugo and Muddle ⁸
Pentagonally twinned plates			Dahmen and Westmacott ⁷

lattice deformation. The principles of crystallography of transformation and the concept of invariant line⁴ are applied to analyse Ge precipitation in the initial stages. Further, the role of quenched-in excess vacancies in relaxing the transformation strain and their contribution in producing excess volume required is illustrated.

Detailed selected area diffraction (SAD) analysis is carried out to specify the different orientation relationships (OR). The study identifies three new ORs in addition to confirming the earlier reported ones (Table I). A significant contribution of the present study is the identification of the well-known Ban OR associated with square/rectangular plates, *i.e.*,

$$(100)\text{matrix} \parallel (100)\text{Ge}; [010]\text{matrix} \parallel [011]\text{Ge}.$$

The particles form on $\{100\}\text{Al}$ with edges bounded by $\langle 100 \rangle\text{Al}$. Both from the point of minimization of strain energy and interfacial energy this OR emerges as the most favoured one since two of the minimum misfit directions of the type $\langle 100 \rangle\text{Al} \parallel \langle 100 \rangle\text{Ge}$ can define its habit plane. But, experimentally this OR is very rarely observed indicating that it is mechanically not viable.

Hitherto, the cube-cube OR was associated with triangular/hexagonal/truncated triangular Ge plates on $\{111\}\text{matrix}$. The present study identifies another OR for the triangular plates with the same habit, *viz.*,

$$(111)\text{Al} \parallel (111)\text{Ge}; [110]\text{Al} \parallel [211]\text{Ge}.$$

Another interesting finding of the study is the identification of a triangular/truncated triangular plate on $\{100\}\text{Al}$ with the OR similar to that of the long laths on $\{100\}\text{Al}$, *viz.*,

$$(001)\text{Al} \parallel (111)\text{Ge}; [100]\text{Al} \parallel [110]\text{Ge}.$$

The cube-cube OR is often observed associated with interfaces between phases with large lattice-size differences in a number of solid-solid reactions and epitaxial growth. A convincing explanation for this occurrence in Al-Ge system is given by identifying that strain energy minimisation can be achieved by the choice of nearly matching coincident site lattice (CSL) units. This suggestion is applied to explain a few other examples drawn from literature. The other observed ORs are also rationalised on this basis. Interphase faceting in the nucleation and/or initial stages of growth is suggested to be responsible for the plate precipitate with triangular morphology on $\langle 100 \rangle\text{Al}$.

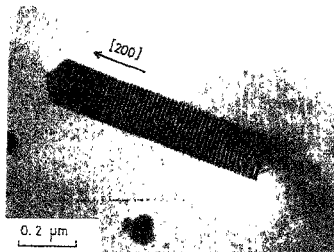


FIG 1 Micrograph showing uniformly distributed interfacial dislocations for the lath-shaped Ge precipitate

A concerted effort is made to characterise the interfacial features experimentally observed at the Al:Ge interfaces associated with the various morphologies by imaging them under specific diffraction conditions. The broad face of Ge laths is shown to be fully coherent in the initial stages under the chosen correspondence and exhibit dislocation loop/moiré fringe contrast after loss of coherency (Fig. 1). The fringe features observed perpendicular to the growth direction on the broad faces and edges are analysed to be interfacial dislocations with $b = a/2(110)\text{Al}$.

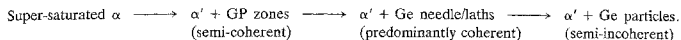
Highly intriguing interphase boundary diffraction contrast images are obtained for the Bain-related Ge plates on $\{100\}\text{Al}$. Parallel arrays of fringe features, perpendicular to the operating g , are observed with available (200) , (220) and (420) -type reflections in $[001]\text{Al}$ zone. The uniqueness of the diffraction conditions makes it very difficult to distinguish between moiré fringes and dislocation arrays for this interface. By imaging under specific diffraction conditions, and analysing the images obtained in different zones, an orthogonal array of dislocations with line direction along $(110)\text{Al}$ and Burgers vector equal to $a/2(110)\text{Al}$ is shown to be associated with the broad face of these plates.

The broad face of the triangular/truncated triangular plate on $\{100\}\text{Al}$ showed a single set of parallel dislocations perpendicular to the minimum misfit direction, *i.e.*, $(100)\text{Al} \parallel (110)\text{Ge}$. The present study indicates the inability to resolve dislocation networks for the Ge plate on $\{111\}\text{Al}$ and for the long rectangular plates on $\{100\}\text{Al}$ with edges along $\langle 110 \rangle \text{Al}$.

The geometrical formulation of Bollmann's O-lattice as developed for centered lattices and the generalised near CSL/DSC lattice model⁹ are used to predict habit planes and dislocation networks. These calculations were carried out considering the germanium lattice as a point lattice, *i.e.*, considering only the fcc lattice framework. For Bain OR the predicted line direction and dislocation spacing are found to be in excellent agreement with those experimentally observed. For the cube-cube OR two nearly matching CSL units could be recognised: a 4:3 Al:Ge with +4.68% misfit and a 7:5 Al:Ge match with residual misfit of -0.52%. The predicted dislocation network is hexagonal and the spacing and strength of Burgers vectors indicate that it would be very difficult to resolve them in diffraction contrast experiments. The same is shown to be the case with the OR of the long rectangular plate morphology. However, resolved dislocations for the lath morphology are very well predicted by these calculations. Finally, group theoretical concepts which are shown to be useful in predicting morphology and number of variants of the product phase in any solid-solid reaction¹⁰ are applied to analyse the Ge precipitates.

4. Conclusions

The edge loops on $\{110\}$ matrix are considered to represent the monolayer GP zone stage in the process of germanium precipitation. Based on findings of the present investigation the following precipitation sequence for decomposition of quenched super-saturated Al-Ge alloy system is suggested:



Three new orientation relationships are identified, the most significant being the well-known Bain relation. Adoption of a near-CSL orientation is considered to result in relatively lower interfacial energy.

The concept of secondary coherent interphase boundary is proposed to characterise the interfaces between phases with large difference in lattice parameter and crystal structure. A comparison of experimental results on the interphase boundary structure and the theoretical 02-lattice analysis shows the validity and usefulness of the near-CSL/DSC lattice concept in the study of interfaces.

In the present investigation it is found that the symmetry of the interfacial dislocation network also has to be considered along with the symmetry of all phases involved in the transformation and the symmetry of any defects that may be involved to explain the observed precipitate morphology.

References

- DLUBEK, G., BRUMMER, O AND HAUTOJARVI, P. A positron study of precipitation phenomena in Al-Ge and Al-Si alloys, *Acta Metall.*, 1986, **34**, 661-667
- RUSSEL, K C. The role of excess vacancies in precipitation, *Scr. Metall.*, 1969, **3**, 313-316.
- OLSON, G. B AND COHEN, M. Interphase-boundary dislocations and the concept of coherency, *Acta Metall.*, 1979, **27**, 1907-1918.
- DAHMEN, U. AND WESTMACOTT, K. H. The role of the invariant line in the nucleation and growth of precipitates, *Proc. Conf. on Solid-Solid Phase Transformations (TMS-AIME)*, 1981, p. 433.
- SOROKIN, L. M. AND SHNIKOVA, A. A. Structural changes in an aluminum-germanium solid solution at the stage of decomposition corresponding to maximum hardness, *Sov. Phys.-Solid St.*, 1968, **9**, 1525-1531.
- KÖSTER, U. Precipitation of germanium from aluminium, *Mater. Sci. Engng*, 1969/70, **5**, 174-176.
- DAHMEN, U. AND WESTMACOTT, K. H. The use of symmetry in the TEM analysis of precipitate morphologies, *MRS Symp. Proc.*, 1986, Vol. 62, p. 217
- HUGO, G. R. AND MUDDLE, B. C. *Precipitate forms in an Al-Ge alloy*, Research report, Monash University, 1986.
- BALLUFFI, R. W., BROKMAN, A., AND KING, A. H. CSL/DSC lattice model for general crystal-crystal boundaries and their line defects, *Acta Metall.*, 1982, **30**, 1453-1470.
- CAHN, J. W AND KALONJI, G. Symmetry in solid state transformation morphologies, *Proc. Conf. Solid-Solid Phase Transformations (TMS-AIME)*, 1981, p. 433.

Thesis Abstract (Ph.D.)

Studies of dynamic elastic properties of spin glass and related magnetic systems across the transition region by Pratip Kr. Mukhopadhyay.

Research supervisor: A. K. Raychaudhuri.

Department: Physics

1. Introduction

This work concerns with audio frequency dynamic elastic measurements in the alloy series $\text{Fe}_{80-x}\text{Ni}_x\text{Cr}_{20}$

through its various magnetic transitions. As x is varied the system goes from ferromagnetic (FM) to antiferromagnetic (AFM) state through intermediate phases of a spin glass (SG) and reentrant spin glass (RSG). Our measurements were focussed on these systems across the transition temperatures of SG and RSG.

Instead of using ultrasonic methods, as was done in the past, to probe magnetic systems across their transition regions (this was extensively done for FM and AFM systems, sparingly for the SG and none for RSG), a low-frequency technique was used here. The use of low-frequency technique not only complements the high-frequency data, but also it is physically more meaningful to compare the low-frequency elastic data with those obtained from susceptibility experiments where only low-frequency measurements are done. This is very important and is one of the principal objectives of the work.

While some elastic measurements were done on SG systems, no work is reported on RSG systems, or the so-called 'mixed phase systems'. This system undergoes a ferro- (or antiferro-) magnetic transition at high temperature, followed by a second transition to spin glass-like state at a lower temperature. This second transition temperature is also called reentrant spin-glass transition temperature (T_{SG}) and is determined from the onset of irreversibility in magnetic measurements. Although some theoretical and experimental works (concerning other properties) are reported recently on them no work has been done so far on the elastic properties of such systems. In these disordered magnetic systems we investigated a physically important question regarding the behaviour of the magnetic domains below T_{SG} . Our experiments very clearly show freezing of the magnetic domains below T_{SG} .

The system chosen was a quasi-binary alloy series $Fe_{80-x}Ni_xCr_{20}$. Here, by varying the alloy composition x the system can be made to go from AFM ($x < 18$ at%) to pure FM ($x > 22$ at%) state through the intervening states of RSG and SG. The change over occurs for a very narrow range of x ($x \approx 20$ at%). The alloys are very suitable for the present work because they facilitate intercomparison of the magnetic systems with different magnetic order and have nearly similar chemical composition and structure. Also, all the species being magnetic the spin-lattice coupling is supposedly higher than in the canonical systems like $AuFe$, $CuMn$, etc. This implies a greater magnetovolume effect for these systems. Also these systems were extensively characterized before. (The last important point for choosing these systems stems from the fact that some of these alloys show an invar-type anomaly and can be successfully explored by the present technique).

2. Experimental method

The dynamic elastic moduli were measured using the so-called 'vibrating reed' apparatus². Here, a thin strip of the sample was clamped to the cryostat at one end. The free end of the reed lied between two electrodes at opposite sides. One of the electrodes carried a signal which excited the reed to vibrate. Typically the voltage was about 5 V and the frequency was matched to the resonance frequency of the reed, which was governed by the geometrical shape of the reed and its elastic modulus which we are concerned with. The other electrode carried high voltage (≈ 120 V) from a battery fed through a high resistor (50M Ω) and connected in parallel to a pair of lock-in amplifiers, one running at quadrature and the other in phase with the signal. A phase-locked loop was made by taking the quadrature output from the lock-in and feeding it to the voltage-controlled oscillator (which generated the signal) through an integrator with variable time constant. This ensured that the system was always at resonance. At resonance the in-phase part gave the amplitude and a frequency counter read the frequency. From these two values the sound velocity and attenuation could be found out.

The whole system was kept under high vacuum ($\approx 10^{-6}$ Torr) in the cryostat. The temperature could be varied from about 1.5 to 270 K and measured by a germanium and a platinum thermometer. A heater

$Fe_{80}Ni_{20}Cr_{20}$: FM alloy; $Fe_{54}Ni_{26}Cr_{20}$: RSGII alloy; $Fe_{27}Ni_{23}Cr_{20}$: RSGI alloy; $Fe_{19}Ni_{21}Cr_{20}$: SG alloy; $Fe_{66}Ni_{14}Cr_{20}$: AFM alloy.

was used for heating. A special low-dissipation four-terminal home-made bridge¹ was used to measure the temperature and another home-made temperature controller maintained the temperature to better than $\pm 0.1\%$. A Helmholtz coil arrangement outside the cryostat was used to measure the elastic properties under magnetic field which could be controlled either manually or by a computer through a home-made magnet controller. Data were acquired by a PC.

Characterization of the system was done by various methods—ac susceptibility, resistivity, x-ray, metalurgical studies.

3. Observations and discussion

- i) For the spin glass ($T_F \approx 16$ K) the sound velocity shows a minimum at temperature $T \approx T_F$ and the attenuation shows a maximum at $T < T_F$. The behaviour for $T > T_F$ can be explained by mean field theories for a paramagnet. But it fails below T_F where a relaxational dynamical theory in the context of frozen spin configuration holds^{3,4}. We have compared this behaviour also with the AFM system ($T_N \approx 26$ K).
- ii) In the ferromagnet ($T_C \approx 140$ K), domain-related contribution can be seen in the elastic moduli. In addition, another contribution comes from the magnetovolume effect. This is reminiscent of the invar problems and we tried to solve it accordingly.
- iii) In the RSGs (RSGI, $T_C \approx 35$ K and $T_{SG} \approx 20$ K; and RSGII, $T_C \approx 56$ K and $T_{SG} \approx 7$ K), domain-related contribution exists for $T < T_C$ which abruptly vanishes just below and T_{SG}^+ . It may mean that the domains get locked for $T < T_{SG}$ which is also confirmed by a recent TEM study⁶. So, at these temperatures the magnetic contribution to the elastic modulus mainly comes from the magnetovolume effect which is similar to that in the spin glass.

The above observations and conclusions seem to have general consequences even if they are made in a particular system.

References

1. MUKHOPADHYAY, P. K. AND RAYCHAUDHURI, A. K. Easy to build 4-terminal ac bridge, *J. Phys. E*, 1986, **19**, 792-796.
2. MUKHOPADHYAY, P. K. AND RAYCHAUDHURI, A. K. A simple vibrating reed apparatus for use at low temperatures, *J. Phys. E*, 1987, **20**, 507-511.
3. MUKHOPADHYAY, P. K. AND RAYCHAUDHURI, A. K. Sound damping at spin-glass transition temperature, *Proc. DAE Symp. on Solid State Phys.*, 1986, Vol. 29C, p. 39.
4. MUKHOPADHYAY, P. K. AND RAYCHAUDHURI, A. K. The elastic manifestation of a spin glass: a low-frequency study, *J. Phys. C*, 1988, **21**, L385-L389.
5. MUKHOPADHYAY, P. K. AND RAYCHAUDHURI, A. K. Dynamic elastic measurements in a reentrant spin glass system through the transition temperatures, *Proc. DAE Symp. on Solid State Phys.*, 1988, Vol 31C, p. 241.
6. SENOSSI, S., HADIUDI, S. AND FOURMEAUX, R. *Phys. Rev. Lett.*, 1988, **61**, 1013-1016.

Thesis Abstract (M.Sc. (Engng))

Effects of some rotor modelling parameters on general trim of helicopter using explicit governing equations by R. S. V. S. Pavan Kumar.

Research supervisor: J. Nagabhusanam.

Department: Aerospace Engineering.

1. Introduction

Most of the dynamic stability investigations of helicopter are based on perturbation equations written

about a periodic equilibrium position. Accurate knowledge of control settings and the corresponding equilibrium state parameters is required to predict reliable rotor blade damping or loads for given flight conditions^{1,2}

Nonlinear differential equations governing rotor blade response together with the equilibrium equations of helicopter are solved numerically by using iterative solution technique to obtain the trim of the helicopter. These methods are numerically intensive and many times their solutions are prone to problems of convergence. On the other hand, trim investigations with explicit governing equations are less computationally intensive and less prone to problems of convergence of solution. Explicit equations of trim are available for simplified analytical models of which the most complex is given by Ryan³.

The analytical model considered in this investigation is advanced with respect to Ryan³ by inclusion of hinge offset, lead lag motions, geometrical twist and root cutout of the blades. Explicit governing equation for trim are derived for this analytical model. Using these equations detailed numerical investigations are carried out to bring out the effects of some of the rotor parameters on the trim solution of helicopter at various flying conditions.

2. Analytical model and its governing equations and solution

A comprehensive general trim analysis of helicopter with coupled rotor-body system is considered. The rotor is modelled as multibladed with rigid flap and lead-lag motions about a coincident offset hinge and hinge-restraint springs. The blade can have root cutout and geometric linear twist distribution. The forces of fuselage in trim equations are represented by its known aerodynamic force and moment characteristics. The aerodynamic forces of vertical and horizontal tails are based on their geometry and aerodynamic parameters. The main and tail rotor inflows are evaluated using the momentum theory.

Algebraic manipulations involved in explicit derivation of governing equations are extremely tedious and manual derivation is prone to human errors. Hence, departing from the conventional manual derivation approach, highly reliable governing equations are derived by a special-purpose symbolic processor DEHIM-II (dynamic equations of helicopter interpretative models-version II). A set of 21 nonlinear algebraic simultaneous equations governing the trim of helicopter are derived in their explicit form. The explicit partial derivatives of the equations required in Newton-Raphson method are also derived by the same symbolic processor. The symbolic output of the equations and derivatives obtained in the form of FORTRAN statements are directly linked as subroutines to the numerical analysis program which solves the governing equations.

No convergence problems were faced in solving the trim equations by Newton-Raphson method. The convergence of solution is very fast. In most cases, the final solution was obtained in less than five iterations. The use of explicit expressions of the partial derivatives of the equations with respect to trim parameters has reduced the computational time substantially and also has avoided some of the numerical computational problems faced when derivatives are obtained by numerically perturbing the trim parameters. The trim analysis program can be run on a personal computer and the average computational time for solving each case of trim is only a few minutes. The program allows to use a smaller set of equations if needed for simplified trim conditions.

3. Results and discussion

Numerical studies are carried out for three cases at various flying conditions. The first two cases correspond to the studies on the influence of improved rotor modelling on trim of helicopter by the inclusion of hinge offset and lead-lag motion of the blade. In the last case, a study on the influence of some of the parameters of helicopter like present angles of horizontal and vertical tail and blade twist on trim is carried out.

The study of inclusion of hinge offset modelling on trim has shown that it can bring about considerable changes in the control pitch settings, fuselage attitudes, blade response parameters and rotor head forces

and moments. Mixed sensitivity is observed with these parameters with the increase of advance ratio. As these parameters have direct bearing on flying qualities, loads and stability of helicopter it is essential to include hinge offset for accurate trim investigation.

The study on inclusion of lag dynamics indicates that some of the trim parameters like cyclic control pitch settings, fuselage roll attitude, cyclic flap and lag response and rotor lateral force and roll moment are influenced by it. The magnitude of changes brought by lag dynamics on many of the trim parameters is basically small. However, for side force, roll moment, roll attitude, longitudinal pitch and lateral flapping the percentage of changes observed is significant. Hence, wherever accurate evaluation of these parameters is necessary, it is essential to include lag dynamics in trim analysis. In the coupled rotor-body stability investigations, lag dynamics plays an important role. As stability needs equilibrium state parameters for a given flight condition, the evaluation of trim with lag dynamics is very much needed for accurate stability investigation. At high advance ratios, depending upon the magnitude of the lag frequency some of the trim parameters can change considerably.

Finally, trim computations are carried out for various preset angles of horizontal and vertical tails and the geometric twist of the blade. The results confirmed the expected trends.

The explicit governing equations and the computer programs for trim analysis can be utilised by helicopter industry.

References

1. DAVID, A
Flap-lag stability of rotor blades in forward flight, *J. Am Helicopter Soc.*, 1975, 20(4), 2-13.
2. SCHRAGE, D. P. AND
PETER, D. A.
Effects of structural coupling parameters on flap-lag forward response on a rotor blade in forward flight using Floquet theory, *Vertica*, 1979, 3(5), 77-79.
3. RYAN, K T
Effect of the fuselage on helicopter trim by an iterative harmonic balance, M.S. Thesis, Sever Institute of Washington University, St Louis, Missouri, Dec. 1983.

Thesis Abstract (M.Sc. (Engng))

Analysis of volume change behaviour of partly saturated soils by B. M. Shashi Kumar.

Research supervisors: T. S. Nagaraj and N. S. Pandian.

Department: Civil Engineering.

1. Introduction

Classical geotechnical engineering principles have evolved mainly in regions of earth dominated by temperate climates. Over the last few decades, the need for engineering and construction has extended on a large scale into much less familiar areas such as tropics. This environment which encompasses many of the developing nations including India has been of major concern due to the magnitude of the projects and the large populations affected.

Since the distinctive characteristics of tropical soils are that they are formed under hot and humid climates, the natural soils in such arid and semi-arid regions and soils subjected to seasonal moisture deficits are in a partly saturated state. India primarily being a tropical country, geotechnical activity in partly saturated soils is inevitable. Further, the mechanics of partly saturated soil is a subject of considerable interest in all the areas of the world where weather conditions are such that there is an annual excess potential of evaporation over precipitation. It is apparent that far more than half of earth's surface is a moisture-deficit area. The problems encountered in partly saturated soils are the intense variability of compressibility and strength from point to point, expansive and collapse soil properties, the frequent

occurrence of very high prestress, etc. These problems are due to changes in the state of soil moisture and their associated changes in the state of soil compatible with external stress conditions.

In view of the above problems, mechanical property characterisation of such a complex system involves arduous, repetitive, time-consuming laboratory investigations. It has always been the fervent desire of geotechnical engineers to evolve simple testing methods, both in the field and in the laboratory, such that with minimum input parameters, the soil behaviour be predicted, within the limits of accuracy desired at engineering level. It has been possible, based on Gouy-Chapman diffuse double-layer theory, to model the volume change and shear strength behaviour of saturated uncemented fine-grained soils by earlier researchers at the Indian Institute of Science. It is attempted in this investigation to extend these principles to model the volume change behaviour of partly saturated uncemented fine-grained soils.

2. Existing literature and physico-chemical considerations

The effective stress approach modified by Bishop¹ was considered to be promising due to its demonstrated success to saturated soil behaviour. However, a critical appraisal of such equations clearly reveals that they are not only complex and deficient exercises but also involve accurate measurement of pore air pressure, pore water pressure and χ , β , β' , ψ factors which is very difficult. More recently, Fredlund and coworkers²⁻³ have advocated the analysis of partly saturated soils by means of independent stress state variables ($\sigma - U_a$), ($\sigma - U_w$) and ($U_a - U_w$). Even here the pore water tension has to be measured for each test condition which is endowed with measurement difficulties and inherent uncertainties. Further, according to Bloch⁴, in an interacting system such as clay-water-electrolyte system, independent continuous stress fields for different phases are not strictly valid and physico-chemical potentials cannot be ignored. Only the overall total stress field is the accepted stress field.

Since it has been established that physico-chemical potentials are important in partly saturated soils, physico-chemical considerations form the basis for this investigation. Since Guoy-Chapman diffuse double-layer theory has formed the basis in the generalisation of saturated soils, the same principles have been extended to analyse partly saturated soils. Negative pore water pressure or tension, which exists as a result of partial saturation, influences the shear strength and compressibility characteristics. Thus the physico-chemical state of pore water is very important in partly saturated soils. This has been well explained by Bolt and Bruggenwert⁵.

For consideration of physico-chemical potentials, state parameter approach has been pursued at the Indian Institute of Science to analyse the behaviour of partly saturated soils

3. Development of the physical model

In the case of saturated soils, during generalisation, void ratio at liquid limit e_L was taken as a normalizing parameter. This is because it is known that liquid limit is the reflection of the surface activity. Further, for all soils at liquid limit water content, the equilibrium state is due to consolidation or suction pressure of 6 kPa and possesses a small shear strength of 1.7-2.0 kPa despite liquid limits varying over several fold. Hence, it is justified in taking e_L as the normalizing parameter. Thus, e/e_L is the generalised soil state parameter for saturated soils. In partly saturated soils, an additional parameter to account for partial saturation has to be incorporated in the generalisation in addition to e and e_L . It has been shown that the pore water tension due to partial saturation can be taken into consideration by the square root of degree of saturation $\sqrt{S_r}$. Thus, $e/e_L\sqrt{S_r}$ forms the generalised soil state parameter in the analysis of compressibility behaviour of partly saturated, uncemented interacting soils.

4. Experimental investigation, results and discussion

For direct application to practice, an engineering model consistent with the analytical model has been generated experimentally. Soils selected in the investigation had such a variation in liquid limit so as to cover the ranges normally encountered in practice. Experiments were conducted for both constant water

content and inundated conditions at two levels: (a) monotonic compression tests, and (b) effect of induced prestress on compressibility behaviour.

In monotonic compression test series, although $e\sqrt{S_v}$ vs $\log p$ plots are distinctly different for different soils, $e/e_L \sqrt{S_v}$ vs $\log p$ plots collapse into a narrow band giving a unique relationship

$$e/e_L \sqrt{S_v} = 0.9830 - 0.2057 \log p$$

with a high correlation coefficient of 0.9161. In the above relationship, $\{(e/e_L) \sqrt{S_v}\}$ is the generalised soil state parameter for partly saturated soils and p the over burden pressure in kPa. This generalised line represents the state line for partly saturated soils. With this generalised state line, it is possible to identify the other compatible states in partly saturated soils.

To examine the validity of this approach, two soils, other than those used in the generalisation, were taken and experiments conducted for both constant water content and inundated conditions. Their behaviour was predicted using the model and the prediction was found to be in agreement with the observed values.

In the effect of induced stress on compressibility behaviour test series, even though $e \sqrt{S_v}$ vs $\log p$ for different soils under inundated condition is different for a particular prestress level, the $e/e_L \sqrt{S_v}$ vs $\log p$ for different soils under inundated condition collapses into a narrow band giving a unique relationship of the form $e/e_L \sqrt{S_v} = a - b \log p$. Further, it was found that the slope of the line joining the inundated points, ρ , was stress dependent and a linear relationship between inundated line slope ρ vs prestress p exists which is of the form

$$\rho = 0.5784 - 0.1559 \log p$$

with a high correlation coefficient of 0.9946.

Further, under constant water content condition, even though $e \sqrt{S_v}$ vs $\log p$ plots were different for different soils for a particular prestress level, the $e/e_L \sqrt{S_v}$ vs $\log p$ plots for different soils under constant water content condition is unique for a particular prestress level. Further, it was seen that the variation in the constant water content condition line slope is almost negligible and an average slope of 0.0367 has been used.

A procedure has been proposed to predict heave or collapse. To examine the validity of the proposed procedure to predict heave or collapse, soils other than those used in generalisation were taken and experiments were conducted for both constant water content and inundated conditions. Since the slope of generalised constant water content line is nearly horizontal, it is suggested, for the sake of simplicity, that the constant water content line be taken as horizontal in the prediction of heave or collapse.

Since the proposed approach is able to predict heave or collapse, it should also be possible to predict swelling pressure for the reason that when a model can predict heave or collapse, there will be a point in the pressure-volume relationship where no heave or collapse occurs which defines the swelling pressure. For this a procedure has been presented.

To examine the validity of this approach to predict swelling pressure, extensive data compiled by Komornik and David⁶ were analysed and found that there is good agreement between the predicted and the actual values.

5. Conclusions

Based on the analysis carried out in this investigation the following specific conclusions can be drawn with relevance to direct practical application.

- (1) The generalised state line for partly saturated soils can be used as an engineering tool to identify other states, i.e., whether cemented, uncemented or prestressed.
- (2) Heave or collapse can be predicted.

(3) Swelling pressure can be estimated.

It is believed that this innovative approach would provide a simple means to analyse and predict partly saturated soil behaviour.

References

1. BISHOP, A. W. *The principle of effective stress. An excerpt from a lecture delivered in Oslo, Printed in Teknisk ukeblad, Norway, 1959, No 39, pp 859-863.*
2. FREDLUND, D. G. *Appropriate concepts and technology for unsaturated soils, 2nd Canadian Geotech. Colloquium, Can. Geotech J., 1979, 16, 121-139.*
3. FREDLUND, D. G. *Soil mechanics principles that embrace unsaturated soils, Proc. 11th Int Conf on SMFE, San Francisco, Vol 2, 1985, pp 465-472*
4. BLOCH, P. *Discussion on stress state variables for unsaturated soils by Fredlund and Morgenstern, J Geotech. Engng, ASCE, 1978, 104(GT2), 303-304.*
5. BOLT, G. H. AND BRUGGENWERT, M. G. M. *Soil chemistry—A. Basic elements, 1976, Elsevier.*
6. KOMARNIK, A. AND DAVID, D. *Prediction of swelling pressure of clays, J. Soil Mech Foundatn Engng, 1969, 95 (SM1), 209-225.*

Thesis Abstract (M.Sc. (Engng))

Simulation of surface profiles due to vapour deposition in straight lines by G. Srinivas.

Research supervisors: M. Satyam and K. Ramkumar.

Department: Electrical Communication Engineering.

1. Introduction

The development of VLSICs (very large scale integrated circuits) is aided by computer tools¹ to analyse, try-err-reentry and capture the design process at various levels — system, behavioural, functional, circuit, gate, device, layout and process engineering. Process and device simulation (which go hand in hand) has become essential² to predict the performance of a device design before the actual fabrication process. The fabrication of an IC includes several surface modification steps on the wafer whose pattern is defined by lithographic masks. Simulation of vapour deposition process is necessary to predict how the thickness of metallisation varies from point to point (profile of deposited film) in the interconnection pattern of VLSI circuits.

To simulate film growth by vapour deposition, several models have been proposed and implemented in process simulators used by IC industry^{3,4}. But their proprietary nature constrains free access for reuse and further development. The models devised so far are restricted to two dimensions and to particular shapes of the substrate (mainly a step shape)⁵. In the present work, an attempt has been made to develop topography simulation software (named ASICDOS) to obtain thickness variations on any given arbitrary surface in three dimensions due to vapour deposition.

If the density of molecules is sufficiently low (as is usual in vacuum conditions of deposition), then it may be assumed that molecules travel without interference throughout their trajectories (either due to physical collisions with other molecules or chemical interactions). The mobility of the deposited material is neglected. The growth of deposition profile is primarily a geometric effect and these assumptions have given good results in the work reported in literature.

With the above considerations, the problem can be stated precisely as follows:

Given

- (i) a surface S , and

- (ii) several point sources O_1, O_2, \dots each of them emitting material with known rates of emission in all directions.

Assuming the material sprayed from each source travels in straight lines throughout its flight and when intercepted by the surface S , sticks on it without sliding;
how to calculate the changed surface profile $S(t)$ after time t ?

The programme ASICDOS takes S and description of sources O_1 to O_n as inputs and computes $S(t)$ and displays it and its thickness profiles graphically at desired time intervals

The solution to the problem is arrived at by the following steps.

- (1) Visibility determination: As each source O 'looks' at S , it can deposit material only on the portion S_0^O of $S(t)$ visible to it. The visible portion S_0^O is determined for each source O_1 to O_n .
- (2) In a small interval Δt , an element ΔS of S grows in thickness due to deposition from only those sources which are visible to it. The net deposition on $\Delta S(t)$ is the sum of the contributions from visible sources. The elements making up $S(t)$ are displaced according to deposition made on them in time Δt to give an incremental change to $S(t)$ resulting in $S(t + \Delta t)$.
- (3) By concatenating the incremental changes on S from 0 up to the time t_1 , due to deposition we get from $S(0)$ the final surface $S(t_1)$ which is displayed along with the thickness profiles over the desired contours.

2. Visibility determination

Determining the visible portion of objects or complementarily the hidden surface removal is a basic problem of computer graphics and therefore we can draw upon and use algorithms from and for graphics. Of the various algorithms available for hidden surface removal, object space algorithms extended to internal visibility are suitable here for determining the visible portion of a surface because the present interest is to go back to the original surface and compute its further properties such as thickness profiles, resistivity, capacitance, etc. So, for the present visibility determination algorithm (VDA), the object surface S is projected on to a unit sphere (globe) located around the observer point O and sweep technique is applied to scan the globe.

3. Plane sweep and VDA

The present algorithm (VDA) modifies the plane sweep to sweep the globe and determines the visibility of the surface and moreover triangulates the visible polygons of S_0^O in the same sweep. Ottman *et al*⁶ applied plane sweep to Boolean masking of polygonal layers by keeping counters for layers in each elementary region and outputting the contours of resulting polygons. Instead, VDA maintains the sorted list of polygonal faces in each elementary region of projected map of S on the globe and by projecting back on to S and assembling the visible portions, marks the visible surface S_0^O and triangulates it in the same sweep using Ghosh's algorithm⁷.

4. Implementation and robust geometric computations

Before displacing according to deposition, each triangle is refined into smaller ones, if deposition on it is not uniform enough. In implementing the algorithms of ASICDOS, robustness is crucial and much effort is spent to tackle degenerate cases and to address issues of robustness.

5. Generative computer graphics and ASICDOS

This program also accomplishes Boolean masking of polygonal layers and triangulation of polygons in space. Unlike the usual algorithms, VDA renders computer graphic images with hidden surface removal, shading and shadowing even when the light sources are placed inside the object, e.g., at the centre of a torus. The phases of Moon are simulated to illustrate shadowing effects from Earth using visibility determination in object space.

6. Testing and validation

The deposition profiles on a torus which is deposited from a spherically symmetric point source placed at its centre are shown. They correspond well with analytic results.

References

- 1 RUBIN, S. M. *Computer aids for VLSI design*, 1987, Addison Wesley.
- 2 LAW, M. E., RAFFERTY, C. S. AND DUTTON, R. W. Simulation of silicon processing, in *Semiconductor silicon* (eds, G. Herbeke and M. J. Shultz), Springer Series in Material Science, Vol 13, Springer-Verlag, 1988.
- 3 NEUREUTHER, A. R., TING, C. H. AND ZU, C. Y. Application of line edge profile simulation to thin film deposition processes, *IEEE Trans.*, 1980, **ED-27**, 1449-1455.
- 4 OLDHAM, W. G., NEUREUTHER, A. R., SUNG, C., REYNOLDS, J. L. AND NANDGAONKAR, S. N. A general simulator for VLSI lithography and etching processes Part II - Application to deposition and etching, *IEEE Trans.*, 1980, **ED-27**, 1455-1459.
- 5 BLECH, I. A. AND VANDER PLAS, H. A. Step coverage simulation and measurement in a dc planar magnetron sputtering system, *J. Appl. Phys.*, 1983, **54**, 3489-3496
- 6 OTIMAN, T., WINDMAYER, P. AND WOOD, D. A fast algorithm for the Boolean masking problem, *Computer Graphics, Vision Image Processing*, 1985, **30**, 249-263.
- 7 GHOSH, S. K. AND MOUNT, D. M. *An output sensitive algorithm for computing visibility graphs*, University of Maryland Technical Report, CAR-TR-302 = CS-TR-1874, July 1987

Thesis Abstract (M.Sc. (Engng))

Sparkover and corona current characteristics of air-gaps and electrostatic precipitator geometry under dc/pulse conditions by B. S. Rajanikanth.

Research supervisor: B. R. Prabhakar.

Department: High Voltage Engineering.

1. Introduction

It is well known that electrostatic precipitators perform poorly with high resistivity dust due to the phenomenon of back corona¹. Modern precipitators have overcome the problem of back corona by superposing pulse voltages on dc². However, there is no universal agreement on the pulse characteristics such as its rise time, width, etc. Hence, an attempt was made to determine the electrical characteristics of precipitator geometry and other basic gaps with dc, and pulses of various rise time and repetition, rate, under clean air conditions, with a view to obtain design information on the pulse-charged precipitators.

2. Experimental set-up and procedure

Experiments were conducted with standard rod-rod and sphere-sphere gap geometries. A prototype wire-plate precipitator geometry was designed which corresponds to the dimensions of one section of industrial precipitator. Helical wires were used for the experiment.

For dc energization, a 250 kV, 25 mA dc set was used. The output voltage was determined by series resistance method. For pulse energization, the following types of pulse generators were designed and developed.

1. A 100-kV millisecond (ms) pulse generator consisting of a series of silicon rectifiers with snubber circuits across them. The output voltage is unfiltered half wave, which was measured using a 100 M ohm resistance divider.
2. A 210-kV nanosecond (ns) surge generator capable of producing pulses of different repetition rates, constructed on the MARX principle, with the normal charging resistors replaced by inductances to provide fast charging.
3. A 100-kV microsecond (μ s) pulse generator based on Masuda's circuit³. In the above two cases, the output voltage was measured using a damped capacitance divider.

The dc + pulse energization was carried out by superposing the nanosecond pulses on to the dc.

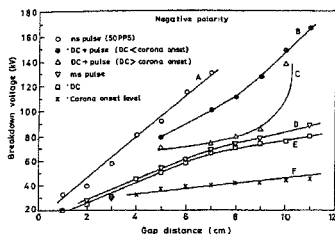


FIG. 1. Sparkover characteristics of rod-gap.

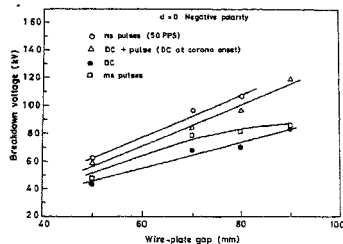


FIG. 2. Sparkover characteristics of wire-plate geometry

3. Results and discussion

Sparkover characteristics of sphere gap with dc and repetitive pulses present a linear relationship between sparkover voltage (SOV) and gap spacings, at both polarities. The SOV was independent of pulse width or repetition rate. The independent behaviour of sphere gap towards various energizations can be attributed to the uniform field existing in the gap.

Figure 1 shows relative effects of various energizations on the sparkover characteristics [SOC] of rod gap at negative polarity. As seen from the figure the *ns* pulse energization results in highest SOV. This is due to the fact that the pulse duration was too short for the streamers to propagate along the gap and cause breakdown. Curve B in the figure shows that the presence of dc decreases the total SOV. A saturation trend is seen with dc and ms pulse energization at larger gap spacings.

Figure 2 shows the behaviour of wire-plate geometry subjected to various energizations at negative polarity. For ms and dc energization, negative SOV was higher than that under positive polarity, whereas for pulse energization, the positive SOV was higher than that under negative polarity. In all cases, single wire/section results in lowest SOV. The studies reveal that pulses of ms to ns duration offer an advantage of higher SOV as compared to dc by nearly 20–60%. The SOV decreases with increase in pulse width, which can be attributed to the low average dc magnitude present in the pulse. Also it has been observed that the SOV decreases with increase in pulse repetition rate which is due to the influence of ionic space charge in the interelectrode space.

An important observation from the V-I characteristics of W-P geometry is that even though pulse operation results in lower magnitude of average dc current, it is possible to operate precipitator with pulse voltages nearly 50% higher than that of dc. The results show that the current density varies linearly with applied voltage for both dc and pulse energizations. Also it varied linearly with the increase in pulse repetition rate and wire-wire spacing.

4. Conclusions

The following conclusions are drawn based on the studies conducted:

1. The SOV of sphere gap is same for dc, pulse and combined dc + pulse energization.
2. No significant change is observed between dc and ms pulse energization. The ns pulse energization results in highest SOV as compared to other energizations.
3. The SOV of rod gap varies linearly with gap spacings for dc and pulse energization. However, for dc + pulse energization, they depend on the dc level and also on the gap spacings.
4. The SOV for W-P geometry increases with decrease in pulse width. The SOV with ms pulse energization is 10–20% higher than that of dc.
5. The SOV of W-P geometry, under pulse energization, at positive polarity is higher than that under negative polarity.

6. The average corona current density under dc is higher than that with pulse energization, for wire-plate geometry.
7. The average corona current density, in case of wire-plate geometry increases linearly with increase in pulse repetition rate and wire-wire spacing.
8. Current density can be varied independent of the dc voltage by varying the repetition rate.

References

1. WHITE, H. J. *Industrial electrostatic precipitation*, 1962, Addison-Wesley.
2. SORENSEN, A. F. Effect of repetition rate on breakdown under repetitive impulse voltages superposed on a dc voltage, *IEEE IAS A. Meet.*, 1985, p. 171.
3. MASUDA, S., OBATA, S. AND HIRAI, J. A pulse voltage source for electrostatic precipitators, *IEEE IAS A. Meet.*, 1978, pp 23-30.

Thesis Abstract (M.Sc. (Engng))

Studies in power conditioning systems for pulsed lasers by P. K. Bhadani.

Research supervisors: M. S. Naidu and D. D. Bhawalkar (Organisation).

Department: High Voltage Engineering.

1. Introduction

Direct current resonant charging and command resonant charging power supply schemes have wide acceptance in laser modulators both in research and industry. These schemes have been used in wide range of average powers. High-energy lasers requiring megawatt average power modulators operating at a few hundred pulses per second (pps) employ these schemes^{1,2}. These schemes are also used in high average power TEA-CO₂ lasers (500 W) operating at 100 pps and requiring 10 kW of average input power³. However, these schemes have certain undesirable features, particularly when high average power is required at moderate pulse repetition rates. The size of the charging choke tends to become larger as the repetition rate becomes lower. At repetition rates of 100 pps and lower, the size of the charging choke becomes comparable to that of the main transformer of the high-voltage dc supply. This makes the overall system bulky. At high average power, a command charge switch is required which has to operate with both anode and cathode at elevated potential thus requiring high-voltage isolation transformers for heaters and grid circuits of the thyatron switch. In addition to these disadvantages, the resonant charger requires a large filter capacitor at the output of the dc supply whose value has to be at least ten times the value of the capacitor to be charged.

In the present work, a laser pulser using a new capacitor charging circuit is proposed. This pulser can operate up to a pulse repetition rate of 100 pps when single-phase 50 Hz mains supply is used. This has several advantages over a resonant charger designed for variable repetition rates up to 300 pps. For example, it does not require a high-voltage filter capacitor, charging choke and command charge switch, thus making the overall system simple, compact and less expensive while maintaining the same high efficiency.

For high pulse repetition rates (~ KHz) another new circuit is proposed which provides high voltage gain, inherent command charge capability and high efficiency. In addition, this circuit offers a simple and compact means for varying the voltage on the capacitor.

2. Circuits studied

Two different types of capacitor-charging circuits proposed in this study are presented and their advantages and limitations discussed.

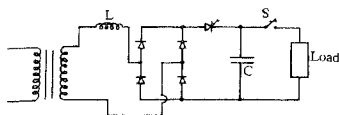
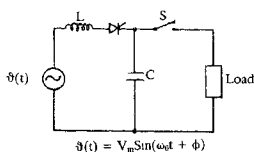


FIG. 1(a). Full-wave capacitor charging circuit with series inductor.



$$v(t) = V_m \sin(\omega t + \phi)$$

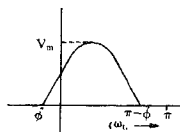


FIG 1(b). Equivalent circuit of fig. 1(a) for analysis.

2.1. Circuit-I

Single-phase version of the capacitor-charging circuit which can operate up to 100 pps is shown in Fig 1. If the presence of inductance L is ignored for the time being, then the capacitor C gets charged to the peak value of the transformer voltage in quarter cycle of the mains supply (*i.e.*, 5 ms in the case of 50 Hz mains). The discharge is timed to take place (with S closed) at the zero-crossing of the charging cycle. For the thyristor (S) to recover, power supply must be isolated immediately following the discharge for a period greater than the deionization time of the thyristor⁴. This is achieved by placing a low-voltage SCR in the charging path (Fig. 1). The SCR operates in the self-breakdown mode. Thus recharging does not take place immediately after the discharge and is delayed depending upon the SCR breakdown voltage and peak of the transformer voltage. This delay is maintained to be more than the deionization time of the thyristor. Thus, the power supply never sees the short-circuited thyristor. The voltage rating of SCR can be calculated from the simple expression

$$V_{scr} = V_m \sin \omega t_d$$

where V_m is the peak value of the transformer voltage and t_d the deionization time of the thyristor. For a peak-charging voltage of 20 kV, a 600 V SCR offers a delay of 100 microseconds, which is more than sufficient for the thyristor to recover.

It is seen from the circuit analysis that the above circuit provides a transformer utilization factor (TUF) of 0.48 only. Thus, for a high average output power the size of the transformer will be larger. TUF is further improved by the series inductance L , which is present in the transformer as leakage inductance. By proper choice of leakage inductance and the recharge delay (ϕ), a high TUF up to 0.9 can be achieved. In the present experimental studies, a TUF of 0.85 has been achieved.

2.2. Circuit-II

Figure 2 shows the diagram of the proposed new circuit for capacitor charging at high pulse repetition rates (kHz). The operation of the circuit is described as follows: Assume that the capacitor is charged from the previous cycle and both switches S_1 and S_2 are open. The grid pulse is applied at S_1 . After a short interval of time (approximately 5 microseconds), another grid pulse is applied at S_2 . After a short interval of time (approximately 5 microseconds), another grid pulse is applied at S_2 . Capacitor C now discharges into the load through S_2 . In the meantime, the power supply is charging the inductor L through switch S_1 . The conduction time of S_1 is kept longer than the recovery time of S_2 . Thus, while inductor L is being charged, switch S_2 fully recovers. After the current in inductor L reaches a predetermined value, switch S_1 is opened by removing the grid pulse. This causes the diode D to become forward

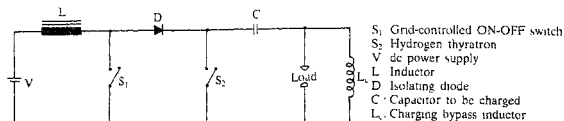


FIG 2. Capacitor-charging circuit for high repetition rate laser pulser

biased, and the power supply and the inductor get connected to capacitor C . Thus the charging energy of the capacitor C is supplied by both the power supply and the stored energy in the inductor. The peak voltage on the capacitor can reach many times the input dc voltage (V) if sufficient energy is stored in the inductor during the switch conduction time of S_1 . After the capacitor C gets charged to the peak voltage, diode D becomes reverse biased and the voltage on C remains at the peak value. Switch S_1 is again turned on, and after a short interval of time, switch S_2 is closed to transfer the energy to the load and the cycle repeats. In the experimental studies conducted, a voltage gain of 20 has been achieved at a capacitor voltage of 1000 V when operating at pulse repetition rates of up to 5000 pps.

3. Conclusions

The present studies have resulted in the development of two new capacitor-charging circuits for laser modulators. Both these schemes have better features than the conventional resonant-charging circuits, and are simple, compact and less expensive while maintaining the same high efficiency as the resonant chargers.

References

- MORIATRY, J. J., HERLING, A. M., CORBIERE, P. A. AND SMOIX, G. K. Multimegawatt modulator designs for minimum weight and volume, *IEEE Conf. Rec. 15th Power Modulator Symp.*, 1982, pp 237-245.
- O' CONNELL, J. C., CARTER, J. AND MCGOWN, J. Upgraded brassboard pulser for HELLS, *IEEE Conf. Rec. 3rd Pulse Power Conf.*, 1981, pp 487-490.
- CHIS, I., CIYRA, A., PRAGNESCUI, V., DRAGANESCU, D., GRIGORESCU, D., GRIGORIU, C., PASCU, M. L., VELCULESCU, V. G. AND ABRUDEAN, M. Design and performance of a high repetition rate TEA-CO₂ laser, *J. Phy. E. Sci. Instrum.*, 1988, 21, 373-376.
- GLASOE, G. N. AND LEBACQZ, J. V. *Pulse generators*, 1965, Dover.

Thesis Abstract (M.Sc. (Engng))

Analytical and experimental studies on the transient linear motion of the pump delivery valve pin of a jerk-pump injection system by A. Vijayan.

Research supervisors: M. V. Narasimhan and A. G. Marathe.

Department: Mechanical Engineering.

1. Introduction

The delivery valve is a vital element of the injection system. Information on actual measurement of the transient motion of the pump delivery valve is not available in literature¹.

Environmental conditions and the limited space constraints render instrumentation for the measurement of the transient motion of the delivery valve difficult. The present investigation is therefore concerned with examining the possible methods of making a reliable measurement of the transient motion of the delivery valve, develop the requisite instrumentation and compare the predicted motion from the analytical model proposed by Srinivasa Murthy² with the measured values.

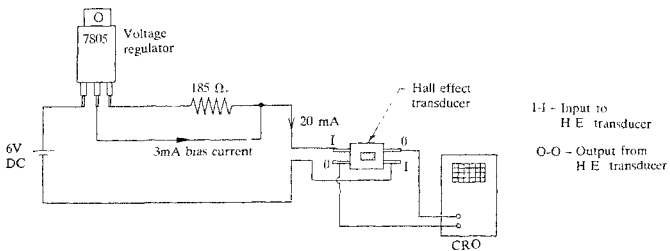


FIG. 1 Circuit diagram of the instrumentation

2. Measurement of transient linear motion

Induced output voltage of an electromagnetic transducer is a function of the rate of change of displacement of the object and the absolute air gap between the object and the permanent magnet core. Hence, static calibration is rendered difficult.

In a capacitive type of transducer static calibration is simple. The output depends on the permittivity of the measuring medium and the area of the capacitor plates. If the measuring medium is an incompressible fluid whose permittivity is relatively low, as in the case under study, the operating voltage has to be relatively high or to compensate for this, the area of the plates has to be more. High voltage and increased area of plates are both undesirable.

In the optical method of measurement the output can be amplified to the desired level and static calibration is possible. Since the output is a function of intensity of light it cannot be used with an opaque medium and signal strength is considerably attenuated in translucent media as in the case under study. Further, the output is generally not linear.

In a linear variable differential transformer the movable soft iron core is coupled to the member whose motion is to be measured. The additional mass of the movable soft iron core would therefore affect the dynamics of the system under study.

Hall-effect transducers are reported to have a linear output³. It is claimed that the amplification of the output to the desired level is possible with low noise level and static calibration is simple. This sensor is sensitive to high temperature and pressure. Under such adverse environmental conditions, however, it offers the advantage of remote sensing in the indirect mode of measurement.

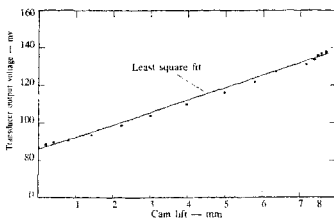


FIG. 2. Calibration curve for validation.

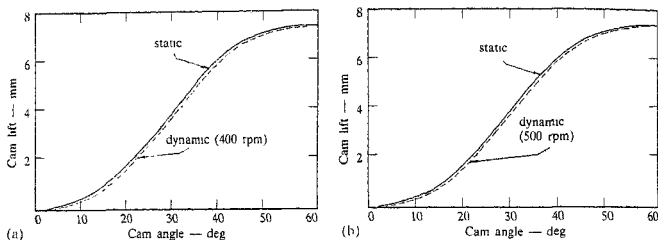


FIG. 3. Comparison of theoretical and experimental cam lifts.

3. Preliminary experiments

The object of these experiments was to try the Hall-effect principle in the indirect mode in a simpler situation. A rig was set up to measure in the indirect mode, the reciprocating motion produced by a cam. A small piece of permanent magnet, about 3% of the mass of the roller tappet and follower, was mounted on the cam follower face and the Hall-effect transducer connected to a constant current power supply (Fig. 1). The output voltage of the transducer was read from a digital multimeter. The calibration curve of lift *versus* change in transducer output voltage with reference to a datum is shown in Fig. 2. The actual displacement curve of the cam is compared with the experimentally determined curve (Fig. 3). It is observed that agreement between the static and dynamic measurements is accurate to better than $\pm 1.5\%$.

4. Measurement of delivery valve pin motion

The maximum weight of a magnet that can be used in the present study is severely limited in view of the low weight (5 to 15 g) of the delivery valve pin. A heavy magnet would inevitably affect the motion of the delivery valve pin. The choice is therefore limited to a light and powerful magnet.

Magnets made of cobalt with rare-earth elements such as samarium-cobalt belong to this new class of permanent magnets with magnetic properties far superior to those of ferrite and Alnico magnets. Samarium-cobalt magnets are 4-6 times more powerful than ferrite and 11.5 times more powerful than Alnico. Further, samarium-cobalt magnets retain their magnetic flux over considerably longer periods.

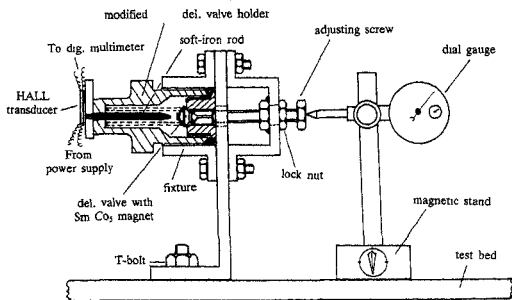


FIG. 4. Static calibration set-up.

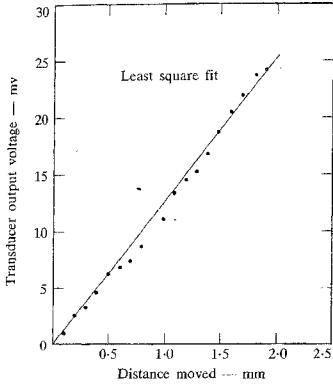


FIG 5 Calibration curve

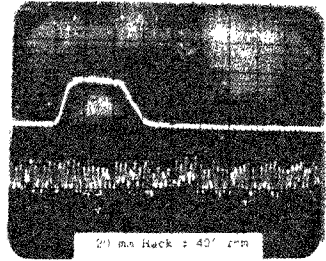


FIG 6 Typical sensor output vs crank angle

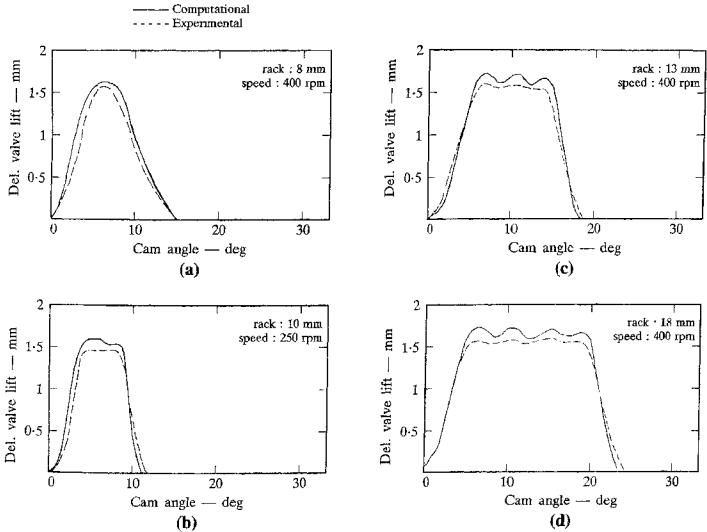


FIG. 7. Comparison of experimental and computational delivery valve lifts

Table I
Measured delivery lift vs crank angle

Rack: 20 mm 1 cm = 15mV Speed: 400 rpm

<i>Cam angle (deg)</i>	<i>Transducer output voltage difference (mV)</i>	<i>Displacement of delivery valve (mm)</i>
1	1.1	0.10
2	2.5	0.20
3	5.1	0.46
4	10.0	0.90
5	15.5	1.30
6	20.6	1.60
7	21.0	1.63
8	21.0	1.63
9	20.6	1.60
10	20.6	1.60
11	19.4	1.56
12	21.0	1.63
13	20.6	1.60
14	19.4	1.56
15	20.6	1.60
16	21.0	1.63
17	20.6	1.60
18	19.4	1.56
19	20.6	1.60
20	19.4	1.56
21	19.4	1.56
22	19.4	1.56
23	19.4	1.56
24	19.4	1.56
25	19.4	1.56
26	19.0	1.50
27	17.5	1.43
28	11.0	1.00
29	8.8	0.83
30	7.0	0.70
31	6.7	0.60
32	6.0	0.50
33	3.8	0.33
34	2.5	0.20
35	0.0	0.00

4.1. Calibration

Corresponding to the geometry of the modified pump delivery valve holder, mounting of the samarium-cobalt magnet on the delivery valve pin and the location of the Hall-effect transducer, a test set-up was fabricated to calibrate the transducer (Fig. 4). The calibration curve is shown in Fig. 5.

4.2. Results

An instrumented Mico 14-mm jerk-pump injection system was run over a range of speeds from 200 to 500 rpm and discharge/cycle of 100 to 600 cu mm. At each camshaft speed, photographs of the transducer output voltage as a function of cam angle were obtained from a double-beam Systronics oscilloscope. Output voltage vs cam angle and the corresponding computed results for a typical test condition are presented in Table I.

Transient motion of the pump delivery valve pin determined by using a Hall-effect transducer in the indirect mode at different test conditions is shown in Fig. 7 and compared with corresponding diagrams evaluated by using the computer code developed by Srinivasa Murthy. The agreement between the predicted and measured delivery valve pin diagrams is consistently excellent.

5. Conclusions

The principle of Hall-effect in the indirect mode of measurement offers an elegant and reliable technique for measuring the transient linear motion of the pump delivery valve pin of a jerk-pump injection system. Further, comparison of measured and computed delivery valve pin displacement diagrams validates the analytical formulation and computer code developed by Srinivasa Murthy for evaluating pressure-time phenomena in a jerk-pump injection system discharging into the ambient.

References

1. BURMAN, P. G. AND DELUCA, F. *Fuel injection and controls for internal combustion engines*, 1962, The Technical Press, London.
2. SRINIVASA MURTHY, N. *Analytical simulation of the pressure-time phenomena in jerk-pump fuel injection system*, Ph.D Thesis, Indian Institute of Science, Bangalore, India, 1978.
3. EPIFANOV, G. I. *Solid state physics*, 1979, Mir Publishers, Moscow.

Thesis Abstract (M.Sc. (Engng))

A numerical simulation of laser melting of alloys by S. V. Raghurama Rao.

Research supervisor: J. Srinivasan.

Department: Mechanical Engineering.

1. Introduction

Lasers have been used in manufacturing processes since early 70s. In recent years, the study of heat transfer and fluid flow in laser melting has received more attention to characterise the temperature structure in the melt. Hsu *et al*^{1,2}, Kou *et al*^{3,4} and Sekhar *et al*⁵ presented numerical models of laser melting, but had neglected the effect of convection. Majumder and Steen⁶, Chan *et al*⁷⁻⁹ studied laser melting process but had neglected latent heat effects. Srinivasan and Basu¹⁰ analysed laser melting in a rectangular cavity and showed the importance of thermocapillary flow. Oreper and Szekely¹¹ and Kou and Sun⁴ studied the effect of convection in melting of alloys during arc welding. Arc welding differs from laser melting in that electromagnetic fluxes influence the flow patterns during arc welding. In this work, a finite difference model of laser melting of alloys is developed, including convection and latent heat effects.

2. Contribution of the thesis

The physical model with coordinate system is shown in fig. 1. Three domains are considered, viz., liquid zone, solid zone and two-phase mushy region. A Gaussian heat flux is assumed to impinge on an initially solid block of alloy. Vorticity-stream function approach is used for solving momentum equations. The dimensionless governing equations are

$$\text{Ste } r \frac{\partial \theta}{\partial \tau} + Ma K \left[\frac{\partial}{\partial r} (r U \theta) + \frac{\partial}{\partial z} (r V \theta) \right] = \frac{1}{C_p} \left[\frac{\partial}{\partial r} \left(r k \frac{\partial \theta}{\partial r} \right) + \frac{\partial}{\partial z} \left(r k \frac{\partial \theta}{\partial z} \right) \right] \quad (1)$$

$$\frac{Ste r^2}{Ma K} \frac{\delta \zeta}{\delta \tau} + r^2 \left[\frac{\delta}{\delta r} (r U \zeta) + \frac{\delta}{\delta z} (r V \zeta) \right] = \frac{1}{Re} \left[\frac{\delta}{\delta r} \left(r^3 \frac{\delta \zeta}{\delta r} \right) + \frac{\delta}{\delta z} \left(r^3 \frac{\delta \zeta}{\delta z} \right) \right] + \frac{Gr}{Re^2} \frac{(T_1 - T_0)}{\Delta T} r \frac{\delta \theta}{\delta r} \quad (2)$$

$$\frac{\delta}{\delta r} \left(\frac{1}{r} \frac{\delta \psi}{\delta r} \right) + \frac{\delta}{\delta z} \left(\frac{1}{r} \frac{\delta \psi}{\delta z} \right) + r \zeta = 0 \quad (3)$$

where $Ste = C_p(T_1 - T_0)/\Delta h$, $Ma = Re Pr$, $Gr = g \beta \Delta T \rho^2 r_b^3 / \mu^2$, $\theta = (T - T_0)/(T_1 - T_0)$, $\tau = Ste Fo$ and ΔT is the maximum temperature difference in the melt, r_b the laser beam radius, used as the reference length, K and C_p are non-dimensionalised with the solid values. The reference velocity used is

$$\bar{U} = \left| \frac{\delta \sigma}{\delta T} \right| \frac{(T_1 - T_0)}{\Delta T} \text{ for thermocapillary flow and } \bar{U} = \frac{\mu}{\rho r_b} Gr^{1/2} \text{ for buoyancy-driven flow.}$$

Conductivity is assumed to vary linearly in the mushy zone. An effective specific heat $C_p = 1 + \Delta h/(\theta_1 - \theta_2)$ is used in the mushy zone. The fluid flow is assumed in liquid zone only. The boundary conditions are

$$\text{at } r = 0, \delta \theta / \delta r = \delta \zeta / \delta r = 0$$

$$\text{at } z = 0, \zeta = \frac{1}{r} \frac{\delta \theta}{\delta r}; \quad \frac{\delta \theta}{\delta z} = -\frac{q r_b}{k k_s (T_1 - T_0)} - \frac{h_1 \theta r_b}{k k_s}$$

where $h_1 = h_{rad} + h_{conv}$, and $q = q_0 \exp(-3r^2)$ at $r = R/r_b$, $\theta = 0$; at $z = L/r_b$, $\delta \theta / \delta z = 0$, $\psi = 0$ along all boundaries.

At the liquid-mushy boundary, vorticity is derived by assuming a quasi-stationary, no-slip interface. Alternate direction implicit (ADI) method and successive over relaxation (SOR) scheme are used for solving the equations. The thermophysical property values are taken from Oreper and Szekeley¹¹ and Kou and Sun⁷.

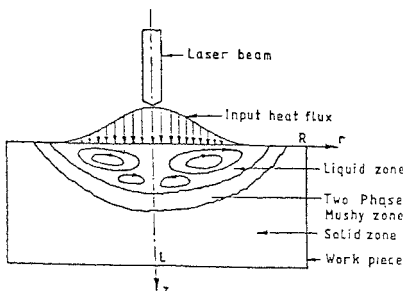


FIG. 1(a). Physical model of laser melting.

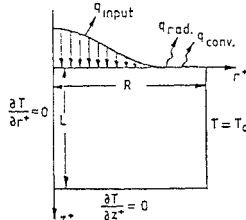


FIG. 1(b). Boundary conditions used.

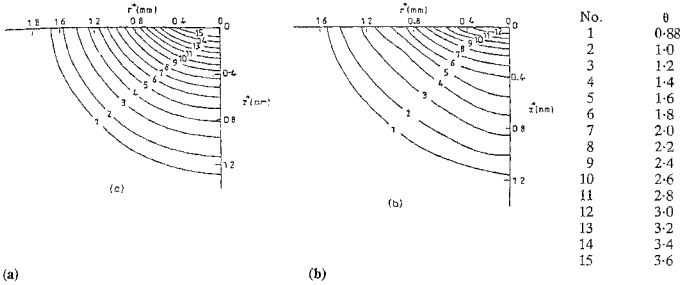


FIG. 2. Isotherms for (a) conduction and (b) convection for aluminum alloy with $r_b = 1.5$ mm.

3. Results

A 20-kW cW laser is assumed to impinge on a flat surface. The absorptivity of aluminium alloy is assumed to be 14%. Same amount of absorbed heat flux is used for steel. The isotherms for the case of pure conduction and with thermocapillary flow included are shown in Fig. 2 for aluminium alloy. The isotherms are distorted and the depth slightly decreased when the fluid flow is included, showing the effect of convection. The flow pattern, as shown in Fig. 3, indicates two contra-rotating cells. The primary cell, near the pool surface is stronger, as can be seen from the stream function values. This stronger primary cell brings cold fluid from the bottom to the top, thus reducing the temperatures near the line of symmetry, and hence the depth. On the free surface, the surface tension being higher near the periphery, the liquid is pulled towards the periphery. Thus flow is radially outward. In the case of steel, the distortion of isotherms is larger (Fig. 4). The decrease in depth when convection is included is also more in steel. Hence, the effect of convection is more important in steel. This is also indicated by the fact that Pr of steel is 30 times higher than that of aluminium alloy.

This study shows that during laser melting of alloys, convection plays a significant role. The depth of the melt decreases with increasing convection. Width is controlled by heat flux. Buoyance effects can be significant for impure alloys.

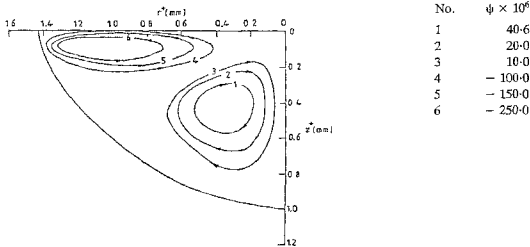
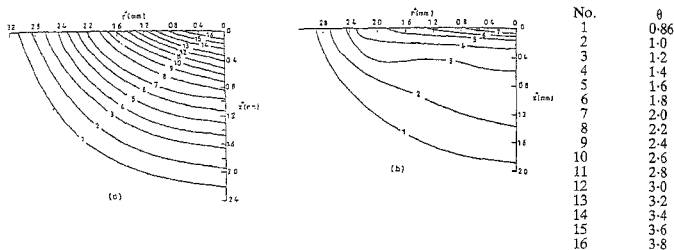


FIG. 3. Streamlines for aluminum alloy with $r_b = 1.5$ mm.



(a) (b)
 FIG 4. Isotherms for (a) conduction and (b) convection with $r_b = 3.0$.

References

1. HSU, S. C., CHAKRABORTY, S. AND MEHRABIAN, R. *Met. Trans. B*, 1978, 9, 221-229.
2. HSU, S. C., KOU, S AND MEHRABIAN, R. *Met. Trans. B*, 1980, 11, 24-28.
3. KOU, S., HSU, S. C AND MEHRABIAN, R. *Met. Trans. B*, 1981, 12, 33-45.
4. KOU, S AND SUN, D. K *Met. Trans., A*, 1985, 16, 203-213.
5. SEKHAR, J. A., MEHRABIAN, R. AND FRASER, H. L. *110th AIME Annual Meeting*, Chicago (eds, Mukherjee, K. and Majumder, J), 1981.
6. MAJUMDER, J. AND STEEN, W. M. *J. Appl. Phys.*, 1980, 51, 941-947.
7. CHAN, C., MAJUMDER, J. AND CHEN, M. M. *In Applications of lasers in material processing* (ed. Metzbowser), 1983, ASM, Metals Park, OH.
8. CHAN, C., MAJUMDER, J. AND CHEN, M. M. *Met. Trans. A.*, 1984, 15, 2175-2184.
9. CHAN, C., MAJUMDER, J. AND CHEN, M. M. ICAELO, 1985.
10. SRINIVASAN, J. AND BASU, B. *Int. J. Heat Mass Transfer*, 1986, 24, 563-573.
11. OREPER, G. M. AND SZEKELY, J. *J. Fluid Mech.*, 1984, 147, 53-79.

Thesis Abstract (M.Sc. (Engng))

Development and evaluation of silicon carbide particulate reinforced aluminium composites by Debashis Dutta.

Research supervisors: K. Chattopadhyay and C. G. Krishnadas Nair (HAL).

Department: Metallurgy.

1. Introduction

Discontinuous metal-matrix composites of high-strength P/M aluminium alloy matrices reinforced with SiC, in particulate or whisker forms, are receiving a great deal of attention for demanding applications in

aerospace and automobile industries^{1,2}. The interest in Al-SiC composites is related to their high and tailorable specific modulus and strength, easy adaptability to conventional metal-working methods, and much less dependence of the engineering properties with direction than with continuous composites.

In view of the high specific strength and modulus, a number of prototype airframe parts have been produced from Al-SiC composites and tested. These composites have also found exciting applications in the automobile industry because of their high wear resistance and low coefficient of thermal expansion.

The present work is devoted to studies on powder metallurgy processing of Al-SiC particulate composites to develop a P/M process suitable for manufacturing these composites for India's aircraft industry. This study was necessary in the absence of published literature on the exact details of P/M process followed for making Al-SiC composites.

2. Experimental work

Composites of pure aluminium matrix reinforced with different volume fractions of SiC particulate (5 to 20 volume per cent) were made by two alternate P/M processing methods.

In the first method, Al-SiC composites were processed by the conventional route of cold compaction and sintering. Al-SiC powder mixes prepared by ball milling were cold-compacted and then sintered in dry nitrogen atmosphere. The sintered billets were then extruded at extrusion ratios of 4 and 6.25. The processing variables studied and optimised, during the experiments, were mixing time, ball-to-charge ratio of ball milling, compaction pressure, and sintering and extrusion temperatures. The effect of these variables on powder characteristics, microstructure and mechanical properties was studied.

In the second method, Al-SiC composites were prepared by encapsulating the powder mix in specially designed aluminium cans, vacuum degassing the canned powder mix for 1 hour at a pressure of 2×10^{-5} Torr and a temperature close to the subsequent hot-working temperature and then hot-pressing the vacuum degassed mix in an available extrusion container fitted with a blind die. Hot-pressing load was varied to obtain 100 per cent density billets. The billets were then decanned by machining and extruded at a single extrusion ratio of 14:1.

The Al-SiC extrusions made by the two P/M methods were compared and the optimum P/M processing parameters established through comparative assessment of mechanical properties, microstructure and tensile fracture characteristics. The effects of SiC volume fraction and particle size and extrusion ratio on mechanical properties and microstructure were also studied during the investigation.

After establishing the optimum P/M processing method, further work was done for developing SiC particulate reinforced composites with a typical high strength 6XXX aluminium alloy as the matrix material. The alloy chosen is a heat-treatable alloy conforming to IS-733-H30, which is a near-equivalent of 6061 aluminium alloy. H30-SiC composites were heat-treated to T6 temper and the mechanical properties assessed and compared with those of similar 6061Al-SiC composites already developed by DWA Composites Specialities, Inc., USA.

3. Results and discussion

The mechanical properties of unreinforced pure aluminium P/M extrusions and of aluminium composites, reinforced with 5 and 15 volume per cent of SiC particles, processed by the two P/M methods, are presented in Table I.

A comparison of the mechanical properties of the SiC particulate-reinforced aluminium composites made by the two different P/M methods, shows significant property enhancements in the composites produced by the P/M route of vacuum degassing and hot-pressing over the composites made by cold-pressing and sintering. The Young's Modulus and percentage elongation of the composites made by vacuum degassing and hot-pressing are, in particular, observed to be considerably higher than those made by the conventional P/M method. For Al-15 volume per cent SiC, for example, the modulus of the composite made by vacuum degassing and hot-pressing is observed to be about 25% higher than the corresponding composite made by cold-pressing and sintering. Moreover, the observed modulus of Al-5 volume per cent

Table I
Mechanical properties of Al-SiC composites

Sl no.	Al-SiC composition process and extrusion ratio	Density (% T.D.)*		Hardness (HB 10)		0.2% PS (MPa)	UTS (MPa)	Elongation (%)	Young's Modulus (GPa)	
		Sintered/Hot-pressed	Extruded	Sintered/Hot-pressed	Extruded				Pre-sent work (E)	Theoretical (E) ³
1.	Unreinforced pure Al. (99.7%) P/M extrusion									
a)	ER6-25 (cold-pressed & sintered)**	98	100	19	25	23	67	28	66.5	70
b)	ER14 (vacuum degassed & hot-pressed)	100	100	25	27.5	29	75	34	71.5	70
2.	Al-5 Vol. per cent SiC									
a)	ER 6-25 (cold-pressed & sintered)	98	99	46	50	97	137	15	76.5	82.9
b)	ER14 (vacuum degassed & hot-pressed)	99.7	100	52	56	106	146	24	81.5	82.9
3.	Al-15 volume per cent SiC									
a)	ER 6-25 (cold-pressed & sintered)	96.6	98.8	51	54	106	146	6	89.5	110.2
b)	ER14 (vacuum degassed & hot-pressed)	99.7	100	55	60	120	156	15	106	110.2

* Percentage of theoretical density.

** ER - Extrusion ratio.

SiC and Al-15 volume per cent SiC, processed by vacuum degassing, is in close agreement with the theoretical modulus values calculated from Tsai-Halpin equation³. The percentage elongation values, representing the ductility of the composites, are also observed to be as much as 60 to 100% higher in the composites made by vacuum degassing and hot-pressing over those made by conventional P/M.

Further studies of microstructure and tensile fracture characteristics on the composites revealed that the prime reason for the considerable improvements achieved in modulus and ductility of the composites made by the P/M route of vacuum degassing and hot-pressing is a much stronger particle-matrix bonding and matrix densification achieved because of a cleaner, gas-free and more cohesive matrix and particle-matrix interface produced by vacuum degassing. The other contributory factors leading to higher mechanical properties in these composites were usage of finer SiC particles of average size of 8 microns compared to relatively coarse SiC particles of average size of 14 microns used for making composites by the conventional method, a closer matching of apparent densities of aluminium and SiC powders used for making composites by the second P/M method and employing a higher extrusion ratio of 14.

Table II
Mechanical properties of H30-SiC composites

<i>Material composition</i>	<i>Hardness (HB 10)</i>	<i>0.2% PS (MPa)</i>	<i>UTS (MPa)</i>	<i>Elongation (%)</i>	<i>Young's Modulus (GPa)</i>	<i>Remarks</i>
1. H30-P/M T6 unreinforced extrusion	99	266	307	11	70	*
2. H30-15 w/o SiC T6 extrusion	110	388	396	6	97.2	*

* (i) Theoretical modulus is 109 GPa, (ii) Modulus of 15 w/o SiC-6061 DWAL composite is 96.5 GPa.

Table II presents the mechanical properties of unreinforced H30 alloy P/M extrusion and H30/15 w/o SiC composite made by the P/M route of vacuum degassing and hot-pressing and extruded at an extrusion ratio of 14. It can be observed that H30-SiC particulate composites developed possess considerably higher strength and modulus over the reinforced H30 alloy without appreciable loss in ductility. The strength and modulus values of these composites were found to increase with increase in SiC reinforcement volume fraction and these properties compare favourably with the corresponding published property levels obtained on similar SiC particulate reinforced 6061 aluminium alloy composite developed by DWA Composite Specialities, Inc., USA.

The high-temperature mechanical properties of the SiC-reinforced composites were also evaluated and a distinct advantage was established. For example, for a short time exposure up to 1 hour, H30-15 w/o SiC composite has a 175°C usable temperature advantage over the unreinforced alloy.

4. Conclusions

1. Silicon carbide particulate-reinforced pure aluminium composites made by the alternative P/M method of vacuum degassing and hot-pressing are micro-structurally superior and possess higher mechanical properties compared to the composites made by cold-pressing and sintering because of the elimination of gas from the matrix material, usage of finer SiC particles, better matching of apparent densities of SiC and aluminium powders and also because of higher extrusion ratio. The modulus values of the composites made by vacuum degassing and hot-pressing were in close agreement with theoretical predictions.
2. Fracture of Al-SiC composites, processed by vacuum degassing and hot-pressing and bearing finer SiC particles of average size of 8 microns was found to be ductile and initiated in the form of tensile voids at the tips of SiC particles of high aspect ratio aligned along the tensile axis and also by cracking of large isolated SiC particles located close to the fracture surface.
3. SiC particulate reinforced H30 alloy composites were found to possess considerably higher mechanical properties compared to the unreinforced H30 alloy. These properties were found to be comparable to the published property levels of similar 6061 Al-SiC particulate composites developed in USA.

References

1. DIVIACHA, A. P., FISHMAN, S. G. AND KARMARKAR, S. D. *J. Metals*, 1981, 33(9), 12-17.
2. FROES, F. H. AND PICKENS, J. R. *J. Metals*, 1984, 36(1), 14-28.
3. NARDONE, V. C. AND PREW, K. W. *Scr. Metall.*, 1986, 20, 43-48.

Thesis Abstract (M.Sc. (Engng))

Grinding media wear studies with respect to Kudremukh iron ore by C. S. Gundewar.
Research supervisors: K. A. Natarajan, U. B. Nayak and K. Satyanarayana (Indian Bureau of Mines).

Department: Metallurgy.

1. Introduction

Ore grinding is a cost- and energy-intensive process in which the wear of balls is a significant practical problem. Over 50,000 tonnes of steel and cast iron is consumed as grinding media every year around the world in the wet-grinding of minerals¹. Grinding is an essential and unavoidable procedure preceding a concentration operation. The total wear of grinding media in mills is contributed by abrasion, impact, corrosion and erosion. It has been reported that grinding media wear is about 5-10 times greater in wet-grinding than in dry-grinding². Wear of grinding balls is a serious problem encountered by the mineral processing industry. Considerable savings in grinding cost could be achieved if the ball wear is reduced even by a small percentage.

Kudremukh hematite-magnetite deposits are known to be one of the largest single deposits of their kind in the world. It is the largest iron ore mine in India designed to produce 22.6 million tonnes of crude ore per year with daily production of run of mine ore of about 82,000 tonnes. Ball mill grinding is an integral part of processing of Kudremukh ore. As the ore treated per day is very high, the wear of balls and subsequent cost due to wear is very high.

The current study was undertaken with the following objectives:

- (i) To investigate the mechanical and metallurgical properties of different grinding ball materials indigenously available.
- (ii) To bring out the various wear mechanisms involved in the dry- and wet-grinding of Kudremukh iron ore under different experimental conditions.
- (iii) To evaluate possible methods to minimise ball wear and suggest remedial measures to mitigate ball wear in industrial ore grinding with special reference to Kudremukh iron ore.

2. Experimental programme

The work has been carried out from a practical point of view. Three types of grinding balls of 25-mm size, namely, cast hyper steel, high-chrome cast iron and EN-31 (forged) supplied by Indian manufacturers were used, which covers a wide range of chemical composition, microstructure and media hardness. While hyper steel and high-chrome cast iron balls were cast, EN-31 balls were forged.

The as received Kudremukh iron ore sample analysed 48.10% Fe and 29.54% SiO₂ which is the major gangue constituent of the ore. The ore was crushed to -10 +30 mesh using jaw-and-roll crusher and vibrating screen. Mineralogical analysis of the ore sample revealed the presence of about 37 per cent hematite, 28 per cent magnetite plus martitised magnetite and 28 per cent quartz which is known to be very abrasive. Stoichiometric calculation based on sulphur analysis indicates that the pyrite content in the sample could be about 0.2 per cent.

Marked ball grinding tests were carried out under different grinding conditions such as dry and wet and environments such as flushing oxygen and nitrogen in the mill to study the ball wear and its mechanisms with and without the ore using all the three types of balls. The effects of continuous grinding and interrupted grinding were also studied with the hyper steel balls in the presence of ore to throw light on different mechanisms of grinding.

The effect of per cent solids on ball wear and grinding efficiency was evaluated with the hyper steel balls. As the ore contains 0.2 per cent pyrite, the effect of addition of pyrite in the range 0.2 to 10 per

cent was investigated using hyper steel and high-chrome cast iron balls. In some studies, sodium nitrite, a corrosion inhibitor, was used to know its role in reducing corrosive wear of hyper steel balls.

Various physico-chemical parameters influencing ball wear in the grinding of Kudremukh iron ore are discussed.

3. Results and conclusions

Results of marked ball grinding tests indicated that the ball wear increased with time and showed a sharp increase for wet-grinding over dry-grinding for all types of balls. Figure 1 illustrates the ball wear (kg/tonne of ore) as a function of time under different grinding conditions for hyper steel balls. In wet-grinding, the ball wear was found to be more in the presence of oxygen followed by closed mill and was the least in nitrogen atmosphere. The wear of EN-31 forged balls also followed the same pattern as hyper steel balls though the magnitude of ball wear was less due to its hardness and microstructure. But the behaviour of high-chrome cast iron balls was found to be different and their wear in an oxygen atmosphere was the least in nitrogen atmosphere. This is attributed to the passivation effect due to the presence of 11.7 per cent chromium in the balls. It is known that with increase in chromium content, wear of grinding media decreases³. Under all conditions of grinding the order of ball wear was hyper steel > EN-31 > high-chrome cast iron.

The efficiency of grinding in terms of product passing 200 mesh was found to be similar for all the three types of balls. The bar chart in Fig. 2 compares the ball wear for all types of balls as a function of 80 per cent product passing 200 mesh, which is used as a measure of grinding efficiency. The ball wear for dry-grinding could not be represented since the product of desired size could not be obtained even after 90 minutes of grinding. It could be seen that a product of 80 per cent passing 200 mesh could

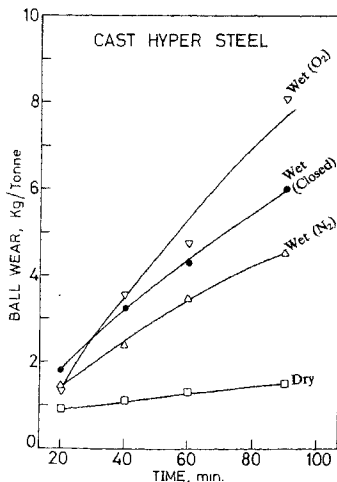


FIG. 1. Ball wear is a function of time under different grinding conditions.

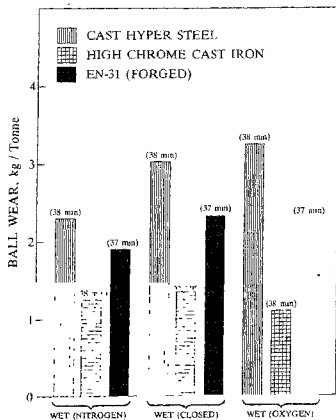


FIG. 2. Bar chart comparing ball wear at 80 per cent passing 200 mesh under different wet-grinding conditions.

be obtained after about 37 minutes of grinding using any of the above types of balls, but the magnitude of wear differs from ball to ball. The results of interrupted grinding against continuous grinding indicate that the impact of corrosive wear is felt more and more as the period of grinding is increased continuously. The order of ball wear under different tumbling conditions in the absence of ore was found to be the same as in the presence of ore but the magnitude of ball wear was much less. It is evident that the ball wear in the absence of ore is mostly abrasive in nature and ball-ball abrasion contributes less towards the total wear. The major contribution comes from ball-mineral abrasion and other factors.

The best results in terms of reduced ball wear coupled with satisfactory grinding efficiency were obtained with 70% solids. Pulp viscosity is known to exert a major influence on ball wear⁴. Abrasive and erosive wear is influenced by the rheological properties of the slurry. The influence of oxygen on the corrosive wear of grinding balls is increasingly felt only if sulphide minerals such as pyrite are also present in the ore. It is reported that the presence of pyrrhotite significantly increased the corrosive wear of mild steel and HCLA steel balls⁵. The corrosive wear of the balls can be reduced to a certain extent with the addition of sodium nitrite, a good inorganic corrosion inhibitor.

Since it may not be practical to change the environmental conditions inside the grinding mill, other acceptable methods to minimise ball wear could be:

- a) To develop proper heat-treatment procedures for the grinding balls to make them better abrasion and erosion resistant.
- b) Design of appropriate cathodic protection methods to reduce corrosive wear of the balls in grinding mills.
- c) Control of alloy composition to achieve good abrasion, erosion and corrosion resistance.

References

1. REMARK, J. F. AND WICK, O. J. Corrosion control in ball and rod mills, Paper No. 121, *Corrosion 76*, NACE, Houston, Texas, 1976.
2. BOND, F. C. Wet versus dry grinding, *Mtn. Cong. J.*, 1957, 43, 38-41.
3. TOLLEY, W. K., NICHOLS, I. L. AND HUIAÏT, J. L. Corrosion rates of grinding media in mill water, 1984, U.S.B.M., RF No 8882, Saltlake City Research Centre.
4. IWASAKI, I., RIEMER, S. C. AND ÖRLICH, J. N. Effect of per cent solids and mill loading on ball wear in laboratory taconite grinding, *Min. Metall. Processing*, August 1985, pp 185-192.
5. NATARAJAN, K. A., RIEMER, S. C. AND IWASAKI, I. Influence of pyrrhotite on the corrosive wear of grinding balls in magnetite ore grinding, *Int. J. Min. Processing*, 1984, 13, 73-81.

Thesis Abstract (M.Sc. (Engng))

Some studies related to quasicrystalline materials by A. Srinivasan.

Research supervisors: E. S. R. Gopal and V. Sasisekharan.

Department: Instrumentation and Services Unit.

1. Introduction

The observation of a coherently diffracting Al-Mn alloy phase with crystallographically forbidden icosahedral ($m\bar{3}5$ or 532) point group symmetry¹ marked the advent of a new class of materials called quasicrystals. Soon alloy systems possessing other crystallographically disallowed rotational axes such as 8-, 10- or 12-fold were also reported. These materials seem to question the fundamental concepts of crystallography by exhibiting long-range order without possessing a periodic lattice. These alloy phases cannot be ignored as curiosities since alloy phases with forbidden rotational symmetries have been observed in many systems such as Al-Li, Fe-Ni, etc., which are of great technological importance.

The two major features that hinder our full understanding of these materials are (1) their minute size (the largest of the stable grains grown so far measure a few millimetres in size), and (2) the presence of crystallographically forbidden symmetry groups. The x-ray diffraction photographs of single grain quasicrystals show very few measurable reflections, from which it is very difficult to deduce the atomic arrangements in these materials. This problem is not yet solved.

Non-periodic tilings^{2,3} help us understand the main features of the diffraction from these materials. These tilings can be generated in 1-, 2- or 3-D and they coherently diffract as shown by their computed Fourier transforms. Projection and the multigrid method are the two most popular ways of generating these non-periodic tilings.

2. Investigations and discussion

In this work, two pieces of work related to quasicrystals have been reported.

The first concerns the estimation of physical properties such as the coefficient of thermal expansion⁴ and linear compressibility. The coefficient of thermal expansion⁴ and the linear compressibility⁵ of rapidly solidified Al-Mn and Al-Fe were reported to be anisotropic. Such an observation is unusual since an icosahedral quasicrystal with $m\bar{3}5$ or 532 point group symmetry is expected to be isotropic. To verify the same, the second- and fourth-rank tensors which represent properties like the coefficient of thermal expansion and linear compressibility, respectively, were subjected to the symmetry operations of the icosahedral (532 or $m\bar{3}5$) and decagonal (10/m or 10/mmm) point groups. These studies clearly revealed that an isolated icosahedral grain or a random conglomeration of icosahedral grains embedded in a glassy matrix cannot give rise to the observed anisotropy in these physical constants. On the other hand, a decagonal grain exhibits transverse isotropy, i.e., a cylindrical isotropy about one axis. Hence, it is possible that the samples used in these experiments^{4,5} might have contained a preponderance of decagonal grains. The presence of decagonal phase and the coexistence of both icosahedral and decagonal phases in these alloy systems are known.

These studies⁶ trigger many derivative questions like the condition under which the icosahedral or decagonal phase forms, their relative abundance at any given alloy composition, etc. This study by itself is a measure of the complexities associated with quasicrystals.

The second piece of work concerns the generation of non-periodic tilings. A careful study of a simple procedure^{7,9} for generating 2-D non-periodic tilings has been made. This method makes use of the self-similarity principle to arrive at the required number of tiles with which one can tile the plane with any required symmetry. This method also uses inflation rules with which the tiling can be generated. The generation procedure is explained taking 5-, 7- and 10-fold non-periodic tilings as examples. To fully understand the diffraction properties of these non-periodic tilings, their Fourier transforms have been computed. Algorithms pertaining to the generation procedure and Fourier transform computations are given in some detail. One interesting aspect of this generation procedure is the possibility of generating more than one tiling with the same n -fold symmetry by using higher order inflation rules. This possibility is exploited to generate three different 10-fold tilings. Once again, the Fourier transforms of these tilings have been computed to facilitate a comparative study of their diffraction properties. These studies reveal that though these tilings have many common features, there are indeed some subtle differences amongst them. Some possible reasons for these observations have been offered.

References

1. SHECHTMAN, D., BLECH, I., GRATIAS, D AND CAHN, J.W. Metallic phase with long-range orientational order and no translational symmetry, *Phys. Rev. Lett.*, 1984, **53**, 1951-1953.
2. GRUENBAUM, B. AND SHEPHERD, C. G. *Tilings and patterns*, 1986, W. H. Freeman.
3. STEDHARDT, P. J. AND OSTLUND, S. *The physics of quasicrystals*, 1987, World Scientific.
4. YOUSUF, M. Comments on so-called icosahedral and decagonal quasicrystals are twins of an 820 atom cubic crystal—Private communication.

- 5 VICTOR JAYA, N., YOUSUF, M.,
RAGUNATHAN, V. S. AND
NATARAJAN, S.
High pressure x-ray studies of quasicrystal Al-18 at.% Fe, *J. Phys. F:Met Phys.*, 1987, 17, L225-L227.
- 6 BALAGURUSAMY, V. S. K.,
SRINIVASAN, A.,
BARANIDHARAN, S. AND
GOPAL, E. S. R.
A note on the observed anisotropy in linear compressibility and thermal expansion of quasicrystals, *J. Phys. F:Met Phys.*, 1988, 18, L105-L107.
7. SASISEKHARAN, V.
A new method of generation of quasiperiodic structures with n -fold axes: Application to five and seven folds, *Pramana*, 1986, 26, L283-L293.
8. SRINIVASAN, A.,
BALAGURUSAMY, V. S. K.,
BARANIDHARAN, S.
SRINIVASAN, A. AND
GOPAL, E. S. R.
A geometric approach to non-periodic tilings with n -fold symmetry, *Proc Solid State Symp C*, Bhopal, 1988, Vol. 31, p. 90
9. SASISEKHARAN, V.,
BARANIDHARAN, S.,
BALAGURUSAMY, V. S. K.,
SRINIVASAN, A. AND
GOPAL, E. S. R.
Non-periodic tilings in 2-dimensions with 4-, 6-, 8-, 10- and 12-fold symmetries, *Pramana*, 1989, 33, 405-420.